1-1-2011

LiDAR-Based Landslide Inventory and Susceptibility Mapping, and Differential LiDAR Analysis for the Panther Creek Watershed, Coast Range, Oregon

Katherine A. Mickelson
Portland State University

10.15760/etd.253

LiDAR-Based Landslide Inventory and Susceptibility Mapping, and Differential LiDAR Analysis for the Panther Creek Watershed, Coast Range, Oregon

by

Katherine A. Mickelson

A thesis submitted in partial fulfillment of the
requirements for the degree of

Master of Science
in
Geology

Thesis Committee:
Scott F. Burns, Chair
William J. Burns
Michael L. Cummings

Portland State University

Abstract

LiDAR (Light Detection and Ranging) elevation data were collected in the Panther Creek Watershed, Yamhill County, Oregon in September and December, 2007, March, 2009 and March, 2010. LiDAR derived images from the March, 2009 dataset were used to map pre-historic, historic, and active landslides. Each mapped landslide was characterized as to type of movement, head scarp height, slope, failure depth, relative age, and direction.

A total of 153 landslides were mapped and 81% were field checked in the study area. The majority of the landslide deposits (127 landslides) appear to have had movement in the past 150 years. Failures occur on slopes with a mean estimated pre-failure slope of 27° ± 8°. Depth to failure surfaces for shallow-seated landslides ranged from 0.75 m to 4.3 m, with an average of 2.9 m ± 0.8 m, and depth to failure surfaces for deep-seated landslides ranged from 5 m to 75m, with an average of 18 m ± 14 m. Earth flows are the most common slope process with 110 failures, comprising nearly three quarters (71%) of all mapped deposits.

Elevation changes from two of the successive LiDAR data sets (December, 2007 and March, 2009) were examined to locate active landslides that occurred between the collections of the LiDAR imagery. The LiDAR-derived DEMs were subtracted from each other resulting in a differential dataset to examine changes in ground elevation. Areas with significant elevation changes were identified as potentially active landslides. Twenty-six landslides are considered active based upon differential LiDAR and field observations.

Different models are used to estimate landslide susceptibility based upon landslide failure depth. Shallow-seated landslides are defined in this study as having a failure depth equal to less than 4.6 m (15 ft). Results of the shallow-seated susceptibility map show that the high susceptibility zone covers 35% and the moderate susceptibility zone covers 49% of the study area.

Due to the high number of deep-seated landslides (58 landslides), a deep-seated susceptibility map was also created. Results of the deep-seated susceptibility map show that the high susceptibility zone covers 38% of the study area and the moderate susceptibility zone covers 43%.

The results of this study include a detailed landslide inventory including pre-historic, historic, and active landslides and a set of susceptibility maps identifying areas of potential future landslides.

Acknowledgements

I would like to thank everyone who has supported, encouraged, and guided me along this journey.

- To my adviser, Scott Burns, for your constant support and motivation. Your enthusiasm for geology inspired my love for landslides.
- To my committee member and DOGAMI co-worker, Bill Burns, for your inspiration to work on this project and your endless guidance and support.
- To my dad and Sandra, for your constant support and motivation.
- To my mom, for inspiring me to become a geologist.
- To my field assistants, Erin Dunbar and Keith Olson, for tagging along and navigating through spider infested treacherous terrain. Bear encounters aside, you guys made it a fun and awesome summer of field work.
- To my committee member, Michael Cummings, for your attention to detail and your guidance.
- To Weyerhaeuser, the city of Carlton, and the City of McMinnville, for access to your land in order for me to field check landslides.
- To the Bureau of Land Management, especially George McFadden, thank you for their involvement in the Panther Creek Cooperative Research Program.
- To my coworkers at DOGAMI, thank you for your assistance, knowledge, and persistent motivation that helped to keep me focused.
- To DOGAMI and the BLM for funding the LiDAR acquisitions.

- To the Panther Creek Cooperative Research Program for allowing me to contribute my work on slope stability.
- To the Association of Environmental & Engineering Geologists (Martin L. Stout Scholarship and Lemke Scholarships) and the Geological Society of America Geology and Science Division (Best Student Paper Award) for their generous support.

Table of Contents

List of Tables

List of Figures

Chapter 1: Introduction

Landslides and debris flows are common in the Oregon Coast Range due to the combination of high precipitation, steep slopes, and in some cases weak, weathered geologic units (Burns, 1998a; Burns et al., 2008). Residing in the northern Coast Range, the Panther Creek Watershed is prone to slope instability. Landslides are common at the contact between marine sedimentary rocks and low permeability volcanic soils on the steeply-dipping slopes (Hoffert-Hay, 2001).

The Panther Creek Watershed is one of six sub-watersheds of the North Yamhill Watershed in Yamhill County, Oregon (Hoffert-Hay, 2001). Major streams in the Panther Creek Watershed include Panther Creek, Falls Creek, Silver Creek, and Russell Creek. The watershed contains three reservoirs including Haskins Creek Reservoir, McGuire Reservoir, and Carlton Reservoir. The Carlton Reservoir, located approximately 11 km west the city of Carlton, supplies the city's drinking water.

Sediments from landslides and debris flows are of great concern in the Panther Creek Watershed due to their effects on water quality. On March 7th 1999, saturated, fractured parent materials created a slip plane that triggered a massive slide that flowed into the Carlton Reservoir (Worrel, 1999). The landslide initiated as an earth flow approximately 8 kilometers (0.5 miles) from the reservoir and mobilized into a debris flow unloading 45,000 cubic meters of material into the reservoir (Pointer, 1999). The landslide resulted in a 50% decrease in the reservoir's capacity, severely affecting the city of Carlton's 1,500 residents (Worrel, 1999).

To help maintain water quality, it is imperative to know where future landslides might occur in the study area. A research group (Panther Creek Cooperative Research Program) sponsored by several organizations, including the Bureau of Land Management (BLM) and the Oregon Department of Geology and Mineral Industries (DOGAMI), has been established and has commissioned the collection of several sets of airborne Light Detection and Ranging (LiDAR) in the Panther Creek Watershed. The LiDAR collected was flown in September, 2007, December 2007, March, 2009, and March, 2010. The LiDAR is currently being used to study hydrology, collect vegetation inventories, assess tree growth, and map soil variation (McFadden, 2010). Other research objectives in the watershed include establishing long-term environmental monitoring stations to study climatic conditions and to quantify precipitation inputs, to access soil chemistry, and to develop an Ecological Site Description for the plant communities in the Panther Creek Watershed. A Soil-Landscape-Climate model also is currently being developed to predict the distribution of soil carbon (McFadden, 2010). In this thesis, the LiDAR datasets were used to create a landslide inventory and susceptibility maps to characterize slope stability.

LiDAR data provide a clear representation of the ground surface since it can penetrate dense canopy common in the Pacific Northwest. LiDAR-derived hillshades, slope maps, and topographic contour lines can be used to identify landslide geomorphology including scarps, toes, and hummocky topography (Schultz, 2004). LiDAR also helps to identify subtle landslide features like debris flow fans and shallow scars at the heads of stream channels (Burns and Madin, 2006). In 2005, a pilot study in Oregon found that compared to other mapping methods, mapping landslides on high-

resolution LiDAR data allows more accurate mapping of the spatial extents of deposits and can result in identification of 3 to 200 times more landslides than other data sets (Burns, 2007).

The aims of this study were to: 1.) create a landslide inventory map of the study area; 2.) create shallow- and deep-seated landslide susceptibility maps for the study area to predict were future landslides may occur according to high, moderate, or low susceptibility zones; and 3.) use differential LiDAR to map active landslide failures in between LiDAR collections. Differential LiDAR subtracts two LiDAR DEMs from each other resulting in a differential dataset to examine changes in ground elevation. These elevation changes can be used to locate active landslides that occurred between the collection dates of the LiDAR imagery.

Chapter 2: Background

2.1 Study Area

The study area is located within the Fairdale 7.5- minute Quadrangle and is situated in the headwater portion of the Panther Creek Watershed in Yamhill County, Oregon. The Panther Creek Watershed resides on the eastern side of the northern Oregon Coast Range near the communities of Carlton and McMinnville (Figure 1). The city of Carlton is located approximately 11 km east of Carlton Reservoir. The study area is approximately 27 km^2, defined by the extent of the LiDAR collected (Figure 2).

Few roads exist within the study area. Main access through the northern portion is by Panther Creek Road, and High Heaven Road is the access to the south. The main road, Von Road, connecting these two roads and traversing the study area became impassible after a landslide took out the road in December, 2007. Other non-maintained roads have been built by the Bureau of Land Management and timber companies for harvesting.

2.2 Climate

The climate of the Panther Creek Watershed is marine-influenced with cold, moist winters and warm, dry summers (Otte et al., 1974). At higher elevations, mean annual precipitation accumulation is between 200-250 cm (80-100 in) and 100-150 cm (40-60 in) at lower elevations with an average annual temperature of 53° F. From November through March, strong rainfall and flooding are common with 70% of the total precipitation occurring in these months (Otte et al., 1974).

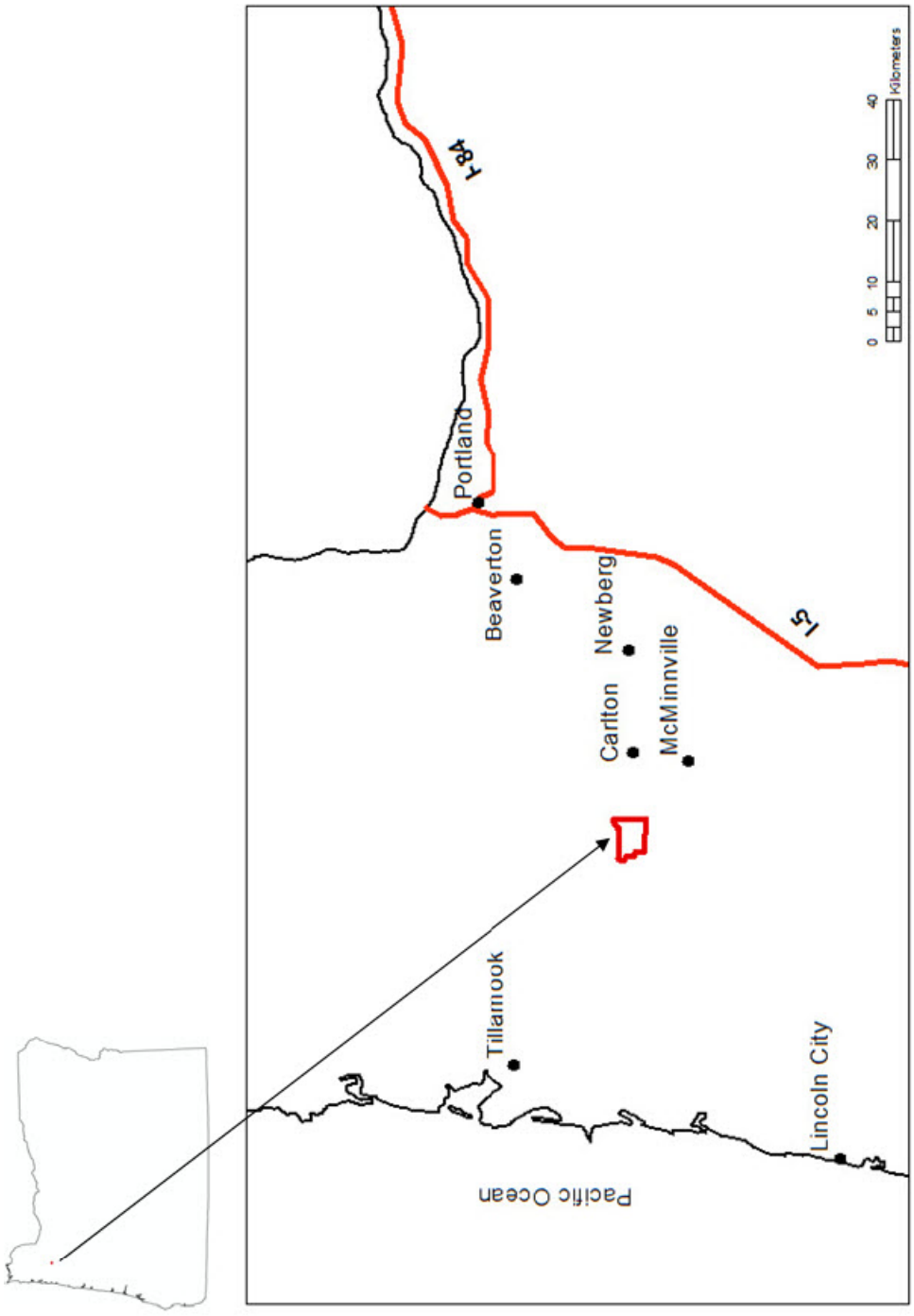

Figure 1. Regional view of study area. Study area is outlined in red.

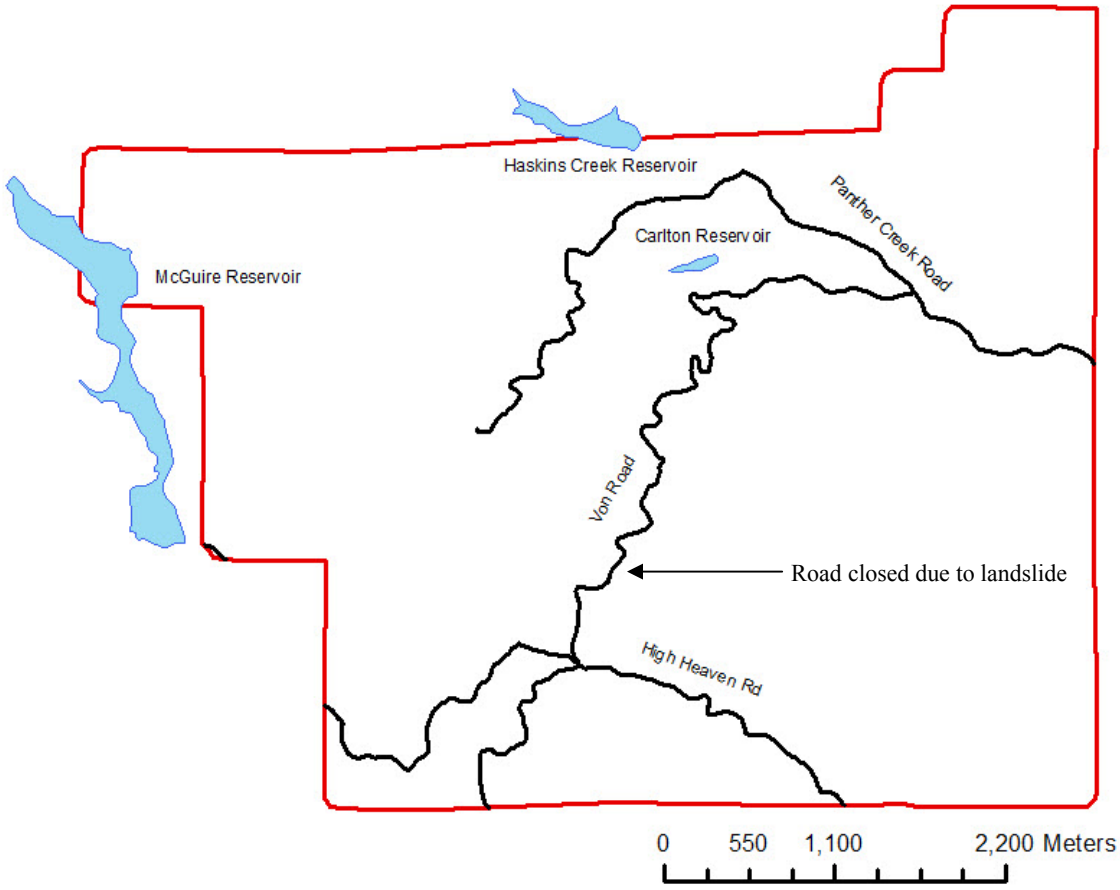

Figure 2. Detailed view of study area. Study area is outlined in red.

2.3 Vegetation

The vegetation primarily consists of second growth Douglas-fir (Hoffert-Hay, 2001) (Figure 3). Other dominant vegetation includes western hemlock, red cedar, and grand fir. Deciduous trees including red alder, cottonwood, and big leaf maple are present in smaller quantities. Alder trees tend to grow in areas that have undergone disturbance. The understory vegetation includes swordfern, Oregon grape, vine maple, salmonberry, salal and devil's club (Hoffert-Hay, 2001).

Figure 3. Typical vegetation in the study area. In the foreground are 8-10 year old Douglas fir trees in an old clearcut. In the background is a mature Douglas fir forest.

2.4 Geology

The geology consists of Upper Middle Eocene Yamhill Formation and Upper Eocene diabase (Figure 4). The regional diabase sill complex is aphyric to plagioclase-phyric with zeolite vesicle fillings (Wheeler et al., 2009). The diabase forms sills with well-developed columnar joints and intrudes the overlying deep-marine strata of the Yamhill Formation (Wells et al., 1994). The contact between the diabase and the Yamhill Formation is poorly exposed beneath thick colluvium of weathered diabase and

sedimentary rocks. The diabase tends to weather to a reddish-orange, clay-rich soil commonly experiences spheroidal weathering (Wheeler et al., 2009) (Figure 5).

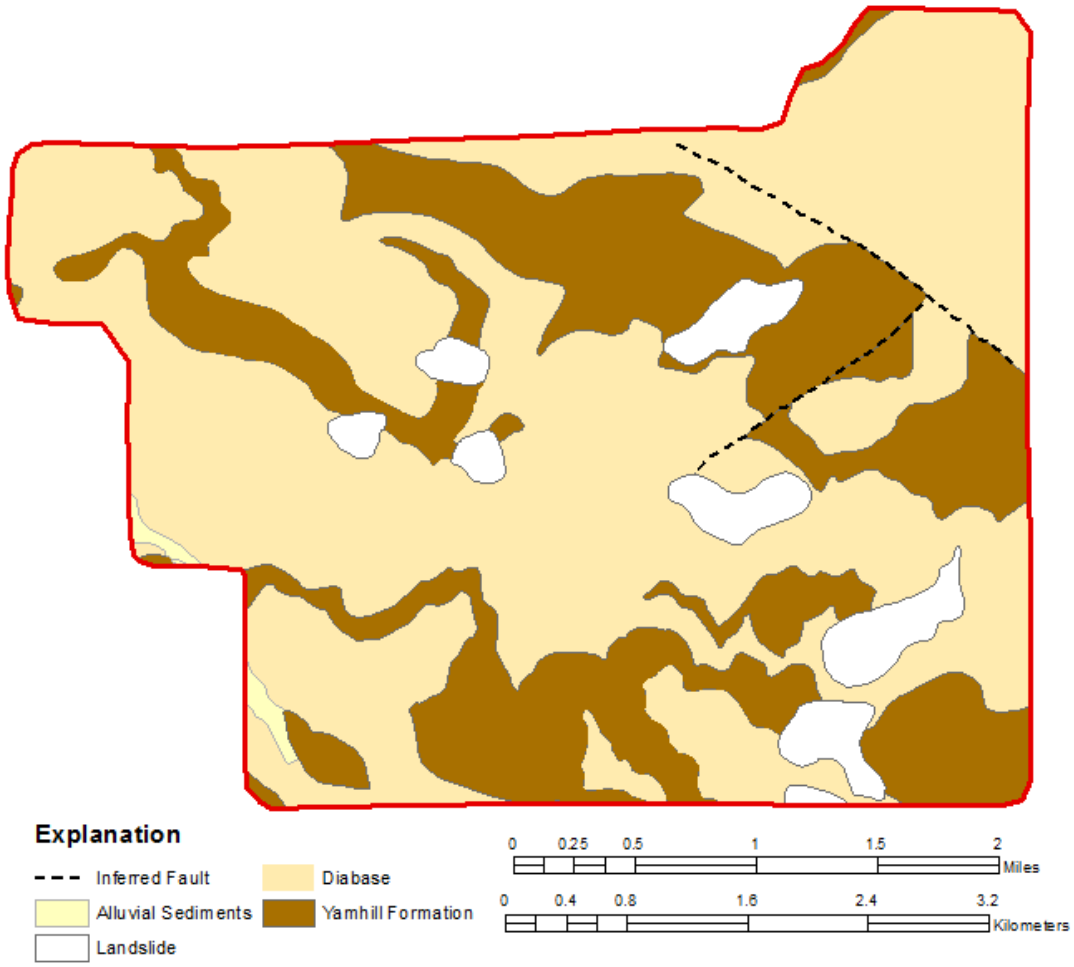

Figure 4. Geology of the Panther Creek study area (Wells et al., 1994).

The Yamhill Formation is comprised of massive- to thin-bedded, dark gray, deep-water marine siltstone commonly containing thin, crossbedded, silicic tuff beds, thin sandstone beds, iron-stained calcareous concretions and carbonaceous plant fragments (Wells et al., 1994; Wheeler et al., 2009). The lower Yamhill Formation is about 150 m (500 ft) thick and is described as dark gray shale and siltstone. The siltstone is the

dominant unit within the study area (Figure 6). The shale and siltstone are overlain by 150 m (500 ft) of thick-bedded fossiliferous sandstone (Orr and Orr, 1999). The sandstone beds are described as arkosic, basaltic, or glauconitic (Snavely et al. 1969). The middle and upper part of the section is described as micaceous, thin-bedded sandstone which is about 1,220 m (4,000 ft) thick (Orr and Orr, 1999). Near the top of the section the Yamhill Formation is interbedded with submarine basalt lapilli breccias of the Upper Middle Eocene Tillamook Volcanics (Wells et al., 1994). The sandstone and Tillamook Volcanics are not found in the study area.

Figure 5. Spheroidal weathering in the diabase.

Figure 6. Siltstone of the Yamhill Formation.

2.5 Pedology (Soils)

Soil data were acquired from the National Resource Conservation Service (USDA-NRCS, 2009). The soils are comprised of well-drained silt loam, clay loam, and silty clay loam soils (Table 1). The dominant four soil series mapped within the study are the Hembre, Melby, Olylic, and Peavine series indicating that the dominant soils are silt

loams (USDA-NRCS, 2009). Taxonomic classifications for each soil series are listed in Table 2.

Table 1. Soil units in study area (USDA-NRCS, 2009; Otte et al., 1974).

Soil Groups	Area mi^2 [km^2]	Percent of Study Area	Description
Dupee, Hembre, Melby, Olyic, Astoria	7.5 [19.3]	79%	Silt loams
Jory, Nekia	1.1 [2.7]	11%	Clay loams
Hazelair, Peavine, Willakenzie, Chehalem, Panther	1 [2.5]	10%	Silty clay loams

Table 2. Taxonomic classification of soil series groups in study area (USDA-NRCS, 2009; Otte et al., 1974).

Soil Group	Taxonomic Classification
Dupee	Mesic Aquultic Haploxeralfs
Hembre	Mesic Andic Dystrudepts
Melby	Mesic Typic Dystrudepts
Olyic	Mesic Typic Haplohumults
Astoria	Mesic Cumulic Haplaquolls
Jory	Mesic Xeric Palehumults
Nekia	Mesic Xeric Haplohumults
Hazelair	Mesic Vertic Haploxerolls
Peavine	Mesic Typic Haplohumults
Willakenzie	Mesic Ultic Haploxeralfs
Chehalem	Mesic Andic Haplumbrepts
Panther	Mesic Typic Haplohumults

2.6 Land Use

Land management is split between federal, city, and private owners, including timber companies. The federally owned land is managed by the Bureau of Land Management (BLM), and the city ownership is split between the cities of McMinnville

and Carlton. Fifty-four percent is privately owned while forty-six percent is publicly owned. The cities own land predominately surrounding the three reservoirs which includes Haskins Reservoir, McGuire Reservoir, and Carlton Reservoir (Burns et al., 2010). The reservoirs provide drinking water for the cities of McMinnville and Carlton.

The study area is heavily managed for timber harvest and management with a short rotation time of 40 to 60 years resulting in even-aged Douglas-fir stands (Hoffert-Hay, 2001). Large portions of the study area have been harvested multiple times since 1900 (Burns et al., 2010). Early stage vegetation is considered between 0-10 years which includes clearcuts and recently planted trees (Figure 3). Mature trees are designated as being between 80-100 years old, and old growth is designated for trees over 200 years old (Hoffert-Hay, 2001).

2.7 Landslides in the Coast Range

Much of Oregon is susceptible to landslides, however, 80% of landslides occur in the western portion of the state due to high precipitation rates (250 cm/yr) and some weak geologic units (Burns, 1998b). Debris flows, earth flows, large rotational landslides, and complex failures are common in the Oregon Coast Range. Landslides are commonly classified according to failure depth: shallow or deep. Shallow- and deep-seated landslides include earth flows, rotational landslides, translational landslides, and complex failures indicating two or more types of movement (Cruden and Varnes, 1996).

The geologic units susceptible to slope instability commonly contain low-strength materials such as clay, shale, loess or weathered rocks (Burns, 1998b). The topography

of the Oregon Coast Range can be described as steep and highly dissected with large-scale slope failures occurring after high precipitation or seismic events (Roering et al., 2005). The steep slopes and high precipitation also initiate earth flows in the weaker sedimentary units in the northern and southern portions of the range. Large rotational and translation slides can occur on paleosols and bedding planes within the sedimentary units (Burns, 1998b). On hilltops and side slopes the soil is typically thin and becomes thicker in valleys. The thick soil layer acts as a source for episodic shallow landslides and debris flows, especially on steep-gradient streams (Roering et al., 2005). Failure at the contact of two geologic units rather than failure within bedding planes of a geologic unit has been found to be a controlling factor in landslide distribution in the Oregon Coast Range (Theule, 2009).

Chapter 3: Methods

3.1 LiDAR

Watershed Science, Inc. (2008) collected airborne-based LiDAR for the Panther Creek Cooperative Research Program. LiDAR was collected in September and December, 2007 for the BLM and in March, 2009, and March, 2010 for DOGAMI. The data sets capture leaf-on (September, 2007) and leaf-off vegetation (December, 2007 and March, 2009) conditions. During leaf-on LiDAR collection, the deciduous vegetation still has their leaves. The resolution of the data was >8 points/m^2 and deliverables included 0.5 m cell bare-earth and highest-hit Environmental Systems Research Institute (ESRI) grids, point cloud Log ASCII Standard (LAS) files, and 0.5 m cell intensity Tagged Image File Format (GeoTIFFS).

3.2 Landslide Inventory Mapping

The March, 2009 LiDAR-derived bare-earth digital elevation models (DEMs) were used to locate and map landslide deposits, flanks, head scarps, and minor scarps. Mapped spatial data entailed a polygon of the mapped landslide deposit, a polygon of the head scarp and flanks, a line of the topmost extent of the head scarp, and lines for minor scarps where applicable (Figure 7). A hillshade map with a sun azimuth of 315° and altitude of 45°, slope map, and 1 m interval topographic contour lines were created from the LiDAR bare-earth DEM using ESRI ArcGIS 9.3 software. Landslides were mapped based on protocol detailed in DOGAMI Special Paper 42 (Burns and Madin, 2009). Landslide features were located by systematically panning through the study area at

scales ranging from 1:24,000 to 1:4,000. Landslides were mapped at a scale of 1:4,000.

Using the LiDAR-derived data, landslide features such as concave slope depression, steep scarps, shear zones along the flanks of a landslide, toes, offset drainages, mid-slope terraces, and hummocky topography were used to accurately delineate landslide boundaries (Schultz, 2004; Burns and Madin, 2009). A June, 2008 QuickBird image provided by the BLM was consulted in addition to the LiDAR data to distinguish between man-made and natural landforms (Burns and Madin, 2009). QuickBird Imagery is taken from a high-resolution commercial earth observation satellite owned by Digital Globe. Figure 8 displays an example of landslide inventory mapping using the 2008 Quickbird imagery and LiDAR derived data.

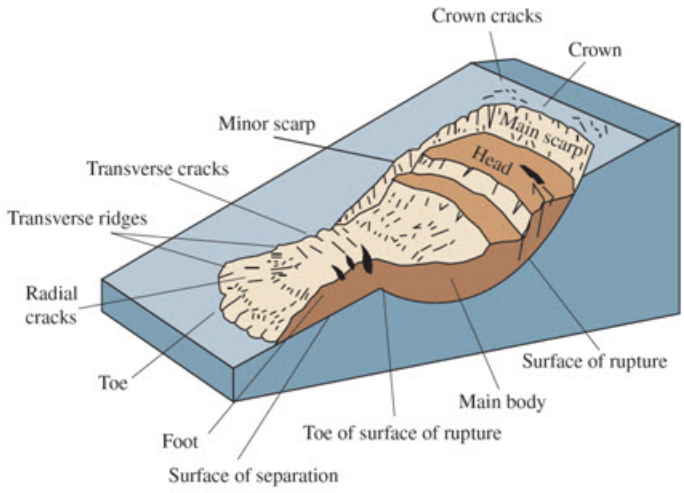

Figure 7. Block diagram of a complex landslide showing common features. For the landslide inventory the main scarp, minor scarps, and main body were mapped (from Burns and Madin, 2009; modified from Highland, 2004)

3.3 Landslide Geodatabase

A landslide geodatabase template from DOGAMI Special Paper 42 was used to store attributes for each landslide deposit (Burns and Madin, 2009). An example of primary attributes for each landslide is recorded in Appendix A. Each landslide was classified as to type of movement (slide, flow, spread, topple, fall, or complex) and type of material (rock, earth, debris) (Table 3). A complex landslide is defined as having two or more types of movement.

Table 3. Landslide classification table for geodatabase from Burns and Madin (2009) modified from Cruden and Varnes (1996).

Type of Movement	Type of Material		
	Rock	Debris	Soil (Earth)
Fall	RF rock fall	DF debris fall	EF earth fall
Topple	RT rock topple	DT debris topple	ET earth topple
Slide-rotational	RS-R rock slide-rotational	DS-R debris slide-rotational	ES-R earth slide-rotational
Slide-translational	RS-T rock slide-translational	DS-T debris slide-translational	ES-T earth slide-translational
Lateral spread	RSP rock spread	DSP debris spread	ESP earth spread
Flow	RFL rock flow	DFL debris flow	EFL earth flow
Complex	C complex or combinations of two or more types (for example, ES-R + EFL)		

The age of each landslide was estimated and attributed as historic (< 150 years) or pre-historic (> 150 years) (Burns and Madin, 2009). Estimation of the landslide age is based on visual inspection of the landslide surface morphology. Historic landslides tend to appear rougher with sharper and better-developed features such as cracks and scarps (McKean and Roering, 2004). Landslide morphology becomes increasingly indistinguishable as features may be subdued or smoothed over time due to natural

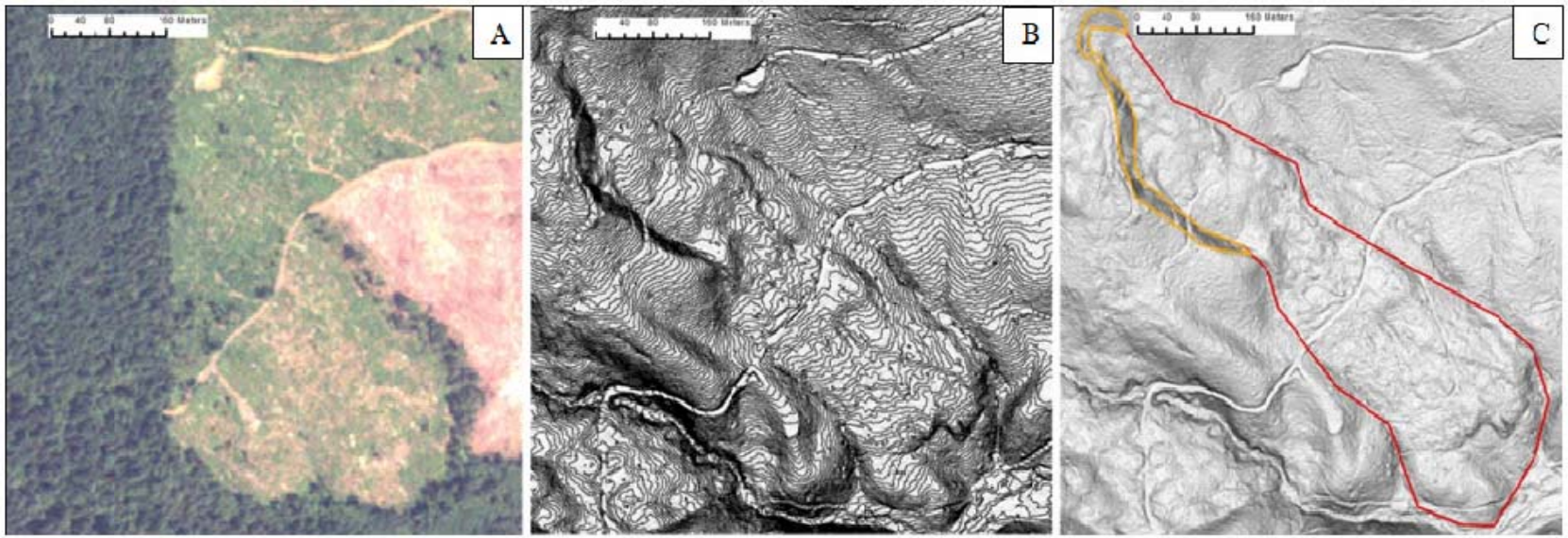

Figure 8. Landslide inventory mapping showing three images of the same area. (*a*) June, 2008 Quickbird image. (*b*) LiDAR derived slope map with 1m contours (*c*) Landslide deposit mapped in red and landslide flanks and scarp mapped in orange

geologic processes, erosion, new landslides, and human activities (Ardizzone et al., 2007). The date of last movement was also recorded if known.

Each landslide was classified according to a confidence level based on the likelihood that the landslide actually exists. This confidence is based on the visual clarity of characteristic landslide features. The clarity of the landslide head scarp, toe, flanks, and internal features (minor scarps, sag ponds, etc.) were ranked 0-10 with zero points for an unidentifiable feature and ten points for a clearly identifiable feature. High confidence was assigned to landslides with > 30 points, moderate confidence was assigned to landslides with 11-29 points, and low confidence was assigned to landslides with < 10 points (Burns and Madin, 2009).

The slope angle (degrees), head scarp height (m) and fan height (m) were measured using the LiDAR-derived slope map and the LiDAR DEM. The head scarp height was measured on the DEM at several locations along the head scarp and the average height recorded. The height of each debris flow fan was measured on the DEM and is the difference in elevation from the bottom to the top of the fan (Figure 9). The slope was measured adjacent to each failed mass in order to estimate the pre-failure slope angle (Burns and Madin, 2009).

Each landslide was then classified as deep- or shallow-seated based upon the slope angle and head scarp height (Figure 10). The equation used to estimate failure depth is:

$$t = x\cos(a) \qquad \textbf{Equation 1}$$

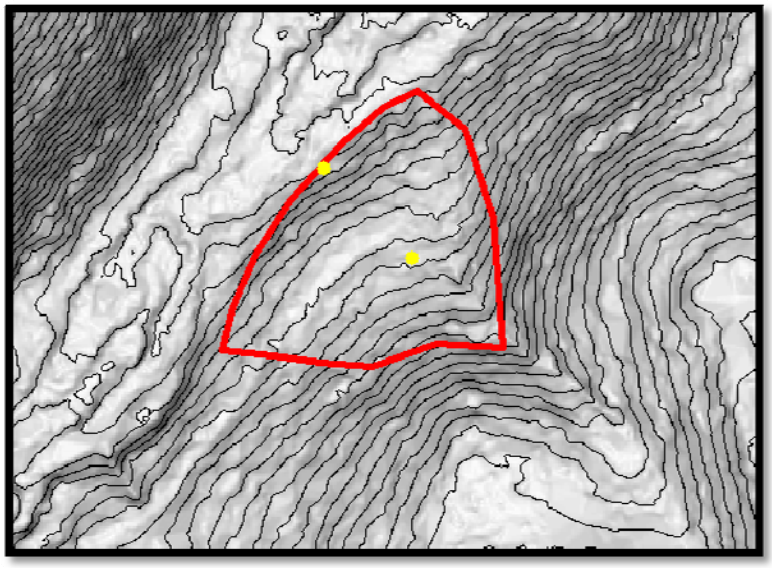

Figure 9. Estimated maximum debris flow fan height is the elevation difference between two points on the top and bottom of the fan. Example measurement locations are shown by the yellow dots (Burns and Madin, 2009).

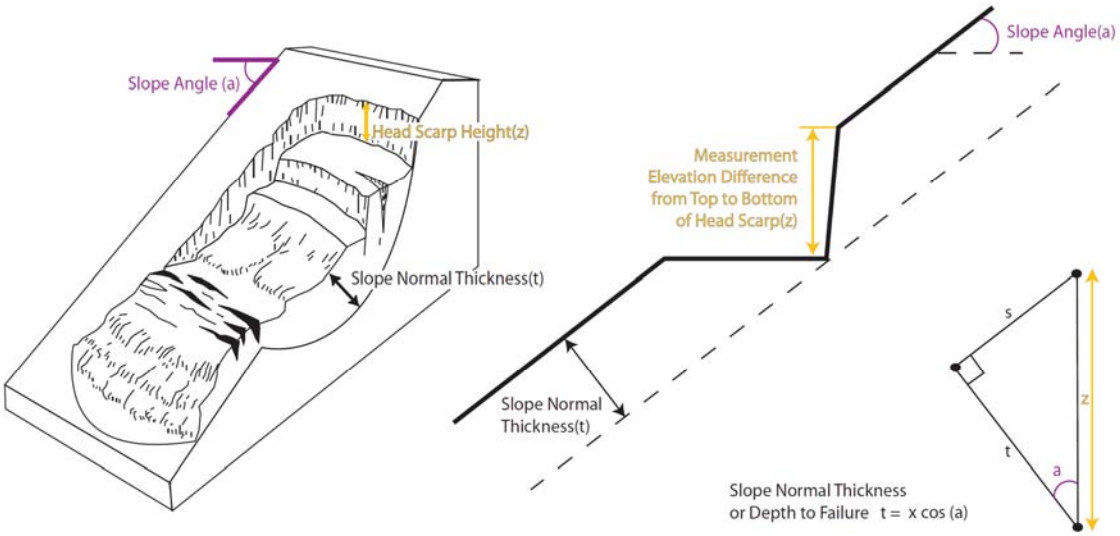

Figure 10. Calculation of estimated failure depth where *t* is failure depth; *x* is head scarp height; and *a* is slope angle in radians. The landslide inventory contains slope angles in degrees that must be converted to radians to calculate estimated failure depth (Burns and Madin, 2009).

Other attributes included in the database are confidence, direction, area and volume. The generalized movement direction is collected as an azimuth (0° to 360°) in increments of 22.5°. The area was calculated automatically in ArcGIS based on the spatial extents of each deposit. The volume was then calculated by multiplying the area by the estimated failure depth for landslide deposits. The volume for debris flow fan deposits was calculated by multiplying the area by one third of the estimated fan height. The geology for each landslide was recorded based on the surrounding geology mapped by Wells et al. (1994) (Burns and Madin, 2009).

3.4 Field Data Collection for Landslide Inventory

The majority of the landslide inventory (81%) was field checked using a landslide inventory sheet. The landslide type of movement, activity, geology, landslide feature present (head scarp, flanks, internal features, toe), land-use, vegetation, and probable cause were recorded following Burns et al. (1998). On active landslides, the length, width, and scarp height also were recorded. Photographs were taken at each landslide deposit. Photographs of each landslide are not included in this thesis due to poor visibility in dense forest canopy. Landslides were identified based upon recognition of landslide features such as scarps, toes, hummocks, colluvium, bent trees, tension cracks, sag ponds, offset drainages, and mid-slope terraces (Figures 11-14).

3.5 Additional Landslide Mapping with Aerial Photography

Aerial photographs from the University of Oregon were scanned. Photos ranged from 1944-2008 and were taken in intervals of 5-7 years. The purpose of looking for landslides on the aerial photos was to identify any landslides missed during the inventory mapping and to give movement dates to some landslides. To identify historic landslides, I looked for distressed vegetation, bare patches of earth, changes in vegetation, and scour along steep drainages (van Westen and Getahun, 2003). Newly found landslides were mapped accurately using the LiDAR derived data sets.

Figure 11. Transverse tension cracks on active landslide. Landslide number PC_87.

Figure 12. Head scarp of the earth flow that silted the Carlton Reservoir in on May 7th, 1999. Landslide number PC_50.

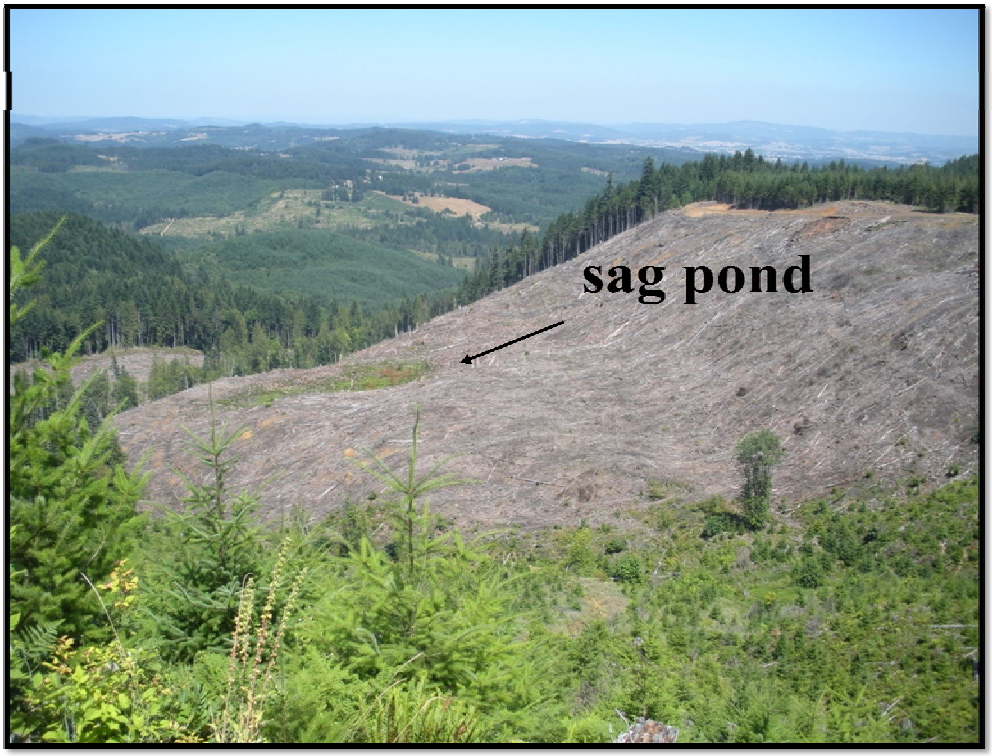

Figure 13. Rotational landslide bench with accompanying sag pond. Landslide number PC_71.

Figure 14. Landslide toe of earth flow PC_93.

3.6 Differential LiDAR: Mapping Active Landslides

The LiDAR collected in the Panther Creek Watershed in September and December, 2007, March, 2009, and March, 2010 cover the same geographic area. The LiDAR data were acquired and processed identically by Watershed Sciences, Inc.. Elevation changes from two of the successive LiDAR data sets (December, 2007 and March, 2009) were examined to locate active landslides that occurred between the collections of the LiDAR imagery.

Burns et al. (2010) began mapping active landslides in the Panther Creek Watershed by subtracting the September, 2007 LiDAR leaf-on from the December, 2007 leaf-off LiDAR data set, resulting in a differential data set. The differential data set displayed negative values indicating a decrease in elevation and positive values indicating an increase in elevation. The results of their differential data set showed elevation changes throughout 98% of the study area. Knowledge of the field area determined that this was a gross overestimate of actual elevation change.

To eliminate the overestimate, several threshold values were tested for the differential dataset to elucidate probable active landslides. The applied threshold values were ± 0.02 m, ± 0.15 m, ± 0.28 m, ± 0.50 m, ± 0.75 m. The ± 0.02 m value was chosen because it was the root mean square error (RMSE) reported by Watershed Sciences (2008) for the LiDAR data. This RMSE value applies to areas with no vegetation cover. The ± 0.15 value was selected since it removed approximately 50% of the overestimation of ground elevation change. The ± 0.50 m threshold value was tested because Burns et al. (2010) found this value to be the overall RMSE for the LiDAR data. Burns et al. (2010) also reported an RMSE of 0.28 m for the differential dataset. The ± 0.50 m and ± 0.75 m thresholds were deemed optimal since they eliminated areas with gross overestimated elevation change while preserving elevation changes that could be associated with slope movement (Burns et al., 2010).

Continuing the work of Burns et al. (2010), this thesis subtracted the December, 2007 leaf-off LiDAR from the March, 2009 leaf-off LiDAR. A ± 0.5 m threshold was applied to the data to eliminate elevation overestimation. Probable active landslides were

mapped based on upon two factors: 1) contiguous positive or negative elevation change in the down-slope direction or 2) the occurrence of negative elevation change in the upslope direction accompanied with a positive elevation change directly below. Burns et al. (2010) applied a third parameter which was the use of imagery taken after the collection of the LiDAR. This third factor was not used in this study since no such imagery existed. Each probable landslide was assigned a high or low confidence based upon the two parameters listed above. High confidence was applied if one or both factors were present (Burns et al., 2010). Probable active landslides were field checked. Confirmed active landslides were added to the landslide inventory database.

3.7 Shallow-Seated Landslide Susceptibility Mapping

Different models are used to estimate landslide susceptibility based upon type of landslide and landslide failure depth. Commonly, shallow-seated landslides are defined as failing above the contact between the overlying soil and bedrock. In Oregon, LiDAR-based landslide inventories have been created for the cities of Astoria, Oregon City, and Silverton (Burns and Mickelson, 2010a, Burns and Mickelson, 2010b, Burns and Mickelson, In Press). The mean estimated failure depths for shallow landslides for these three cities are: Silverton = 2.4 m (7.9 ft), Oregon City = 3.0 m (10.0 ft), and Astoria = 3.1 m (10.3 ft). Based on the findings in these three studies and other studies (Sidle and Ochiai, 2006; Burns, 1999; Burns and Madin, 2009) shallow-seated landslides in this thesis have been defined as having a failure depth less than 4.6 m (15 ft).

To determine shallow-seated landslide susceptibility in the study area, all of the shallow-seated landslides were queried out of the inventory geodatabase and saved to a

separate GIS file. The final shallow-seated susceptibility zones were established based upon locations of shallow-seated landslide deposits and head scarps, factor of safety calculations and buffers following protocol developed by Burns et al. (In Press).

3.7.1 Creation of the Factor of Safety (FOS) Map

Slope stability depends on the ratio of resisting to driving forces. This ratio can be applied to the factor of safety (FOS) against landsliding (Burns et al., In Press) (Equation 2).

$$\text{Factor of Safety (FOS)} = \frac{\text{Total Available Shear Resistance}}{\text{Shear Force Needed for Static Equilibrium}} \qquad \textbf{Equation 2}$$

If the shear resistance is greater than the shear force, the slope would theoretically be stable with a FOS > 1 and would be unstable with a FOS < 1 since the shear force would be greater than the shear resistance. In some cases, all conditions present on the slope may be undeterminable; therefore, a FOS < 1.5 is commonly judged potentially unstable (Cornforth, 2005). In addition, according to the State of Oregon Building code, slope structures normally have to be designed with a FOS > 1.5 (Oregon Residential Specialty Code, R404.5, 2008). Therefore, a FOS < 1.5 is considered potentially unstable in this thesis due to the inability to know all conditions present within a slope (Burns et. Al, In Press).

Two GIS data sets are necessary to create the FOS map: 1) engineering geology and 2) slope. A new geologic map was constructed from Wells et al. (1994) to include

the newly mapped landslide deposits. Landslides mapped by Wells et al. (1994) were modified based off the landslide inventory.

The FOS was calculated for every ½ degree slope for each engineering geology unit in a spreadsheet using the following infinite slope equation

$$FOS = \frac{c+(\gamma z-\gamma_w)cos^2\theta\ tan\phi}{\gamma z\ cos\theta\ sin\theta} \qquad \textbf{Equation 3}$$

where c is the cohesion, ϕ is the angle of internal friction, γ is the saturated soil density (saturated unit weight), γ_w is groundwater density (unit weight), θ is the slope angle, and z is depth to failure surface. Saturated conditions were used to delineate "worst case" scenario. The infinite slope analysis is commonly used for landslides with shallow failure depths where soil lies parallel to the slope surface (Cornforth, 2005).

Because site-specific material properties were not available, a table of general values related to different types of common geologic formations in Oregon was used from Burns et al. (In Press) (Table 5). Once the FOS was calculated, the slope angles corresponding to FOS = 1.5 and FOS = 1.25 were determined for each geologic unit (Qls, Tidb, Ty, and Qf) (Table 4).

Table 4. Slope angles and corresponding FOS for geologic units in study area.

	High Susceptibility	**Moderate Susceptibility**	**Low Susceptibility**
Geologic Unit	**FOS < 1.25**	**FOS < 1.5 and >1.25**	**FOS > 1.5**
Landslide (Qls)	> 11.5°	≤ 11.5° and ≥ 9.5°	< 9.5°
Fill (Qf)	> 12.5°	≤ 12.5° and ≥ 10.5°	< 10.5°
Yamhill Formation (Ty)	> 17.5°	≤17.5° and ≥ 14.5°	< 14.5°
Diabase (Tidb)	> 25°	≤ 25° and ≥ 20°	< 20°

Table 5. General soil and rock material properties from Burns et al. (In Press). Geologic units and associated material properties in study area are highlighted in yellow.

	Common Lithology Description	Common Unit or Formation Names	Common Unit Label	Raster Value	Angle of Internal Friction (ϕ) (degrees)	Cohesion (c) (kPa)	(lb/ft2)	Unit Weight (sat) (kN/m3)	(lb/ft3)
Cohesionless Soils									
Landslide Deposit (shallow failure)	Sheared landslide debris (silts, clays, sands)	Landslide	Qls		10	0	0	19	122
Landslide Deposit (deep failure)	Shearing mainly along deep failure plane	Landslide, colluvium	Qls, Qc	1	28	0	0	19	122
Fill	Sand, silt, gravel, debris mixtures	Artificial Fill	Fill, Qf	2	30	0	0	19	122
Recent Alluvium (fine grained)	Silt, sand	Quaternary Alluvium, loess	Qal, Qf, Ql	3	30	0	0	19	122
Recent Alluvium (coarse grained)	Sand, gravel, boulders	Quaternary Alluvium, gravel fan	Qal, Qcf	4	34	0	0	19	122
Cohessive Soils									
Glacial Till	Sand, silt, clay, gravel	Glacial Till	Qva, Qt	5	34	10	209	19	122
Residual Soil on Igneous Rock	Silty Clay with Boulders	Columbia River Basalt	Tcr, Tidb	6	28	24	501	19	122
Residual Soil on Sedimentary Rocl	Silty Sand, Sandy Silt, Silty Gravel	Troutdale Formation	Tt, Ty	7	30	10	209	19	122

In ArcGIS, the raster calculator tool was used to query the slope angles from Table 4 and the geologic units. Three queries were performed to separate high, moderate, and low susceptibility for each geologic unit. FOS > 1.5 was considered potentially stable, FOS ≤ 1.5 and > 1.25 was considered moderately stable, and FOS ≤ 1.25 was considered unstable. The high, moderate, and low susceptibility units for each geologic unit were combined into a single file to create the FOS map.

3.7.2 Buffers

Since the FOS is calculated based upon a grid type analysis, the result does not take into account the potential impact of adjacent slopes. Due to this limitation, two sets of buffers were applied to the data: 1) 2H:1V buffer on the head scarps of all landslide deposits and 2) 2H:1V buffer on all FOS less than 1.5. A 2H:1V slope is equal to 26° and is equivalent to the minimal angle of internal friction equivalent for most unfailed geologic units (Burns et al., In Press).

The first buffer is applied to the head scarp polygon of each landslide. The area above the head scarp tends to be relatively flat. This low slope angle translates into an area of low susceptibility when the infinite-slope equation is applied. However, the area above the head scarp can fail retrogressively due to a loss of resisting forces. To account for this retrogressive failure, a 2H:1V buffer was applied around each head scarp to increase the susceptibility for these areas (Burns et al., In Press). This buffer is dependent on the head scarp height, so the buffer is different for each landslide. For

example, a landslide with a head scarp height of 3 m (10 ft) will have a 2H:1V buffer of 6 m (20).

The second buffer was applied to areas with a FOS < 1.5. The areas above and below landslide deposits are commonly flat and will have a FOS > 1.5. However, these areas have the potential to be sites of future landslide head scarps and toes. A 2H:1V buffer was applied to areas with a calculated FOS < 1.5 to increase the susceptibility of areas that are potentially unstable (Burns et al., In Press). Since the maximum depth for shallow-seated landslides in this study is 4.6 m (15 ft), the 2H:1V buffer is equal to 9 m (30 ft).

3.7.3 Creation of the Final Shallow-Seated Susceptibility map

The final shallow-seated susceptibility zones (high, moderate, and low) are determined based upon landslide deposit and head scarp locations, calculations of factor of safety, and buffers. Table 6 displays a susceptibility zone matrix describing factors contributing to high, moderate, and low susceptibility zones.

Table 6. Final shallow-seated susceptibility zone matrix displaying factors contributing to high, moderate, and low susceptibility zones from Burns et al. (In Press).

Contributing Factors	Final Susceptibility Zones		
	High	Moderate	Low
1 Factor of Safety (FOS)	less than 1.25	1.25 - 1.5	greater than 1.5
2 Landslide Deposits & Head Scarps	included	—	—
3 Buffers	2H:1V (head scarps)	2H:1V (FOS less than1.5)	—

3.8 Deep-Seated Landslide Susceptibility Mapping

Deep-seated landslides are defined as having a failure depth greater than 4.6 m (15ft). To determine deep-seated landslide susceptibility in the study area, all of the deep-seated landslides were queried out of the inventory geodatabase and saved to a separate GIS file. The deep-seated susceptibility zones were established based upon locations and proximity to deep-seated landslide deposits and head scarps, head scarp buffers, susceptible geologic units, slope angles, and mapper judgment following protocol developed by Burns (2008).

3.8.1 Head Scarp Buffer

Large, deep-seated landslides can move continually (mainly through creep) over time especially during high precipitation events. Reactivation often is focused upslope near the landslide head scarp and at the landslide toe (Burns, 1998b). To account for the retrogressive head scarp failure, a buffer was added to each landslide head scarp polygon. Two different factors were considered for the added buffer. First, a 2H:1V buffer was calculated for each head scarp polygon by multiplying each head scarp height by 2. Second, each deep-seated landslide was reviewed to see if it contained measured minor scarps. The average horizontal distance between all minor scarps was compared to the 2H:1V calculated buffer. The larger of the two numbers was chosen to buffer each landslide head scarp polygon (Burns, 2008).

3.8.2 Susceptible Geologic Units and Slope Angles

The geologic map modified from Wells et al. (1994) (Figure 4) was reviewed to determine which geologic units are susceptible to slope failures. Based on the locations of the deep-seated landslides in the study area, both the Yamhill Formation and highly-weathered diabase are susceptible to deep-seated landslides. The geologic map was viewed with a slope map that contained slopes greater than 10°. This slope angle was chosen since all measured slope angles in the landslide inventory geodatabase were greater than 10°.

3.8.3 Creation of the Final Deep-Seated Susceptibility Map

The deep-seated landslide deposit and head scarp locations and the head scarp buffers were assigned to the high susceptibility zone (Table 7). The boundary between the moderate and low susceptibility zones was mapped free-hand based upon educated mapper judgment. Since all units in the study area are susceptible to landsliding, unfailed areas with slopes greater than 10° were included in the moderate susceptibility zone. Slopes adjacent to identified deep-seated landslides were also included in the moderate susceptibility zone even if they were less than 10°.

Table 7. Final deep-seated susceptibility zone matrix displaying factors contributing to high, moderate, and low susceptibility zones modified from Burns, 2008.

	Final Susceptibility Zones		
Contributing Factors	High	Moderate	Low
Landslide Inventory	Included	-	-
Head Scarp Buffers	Included	-	-
Additional Factors	-	Included	Included

Chapter 4: Results

4.1 Landslide Inventory

4.1.1 Landslide Attributes

Through LiDAR and aerial photography mapping, a total of 153 landslides were mapped in the 27 km^2 watershed (Figure 15) (Table 8) (Appendix C). A review of a GIS inventory of landslides mapped after the 1996/97 storm events (Hofmeister, 2000) showed that two landslides occurred in the study area after a three major storms. These landslides, however, could not be accurately mapped on the LiDAR and were not included in the final inventory. The use of aerial photography added four additional landslides with specific dates of movement and added a date range of movement for one landslide. The four added slides were mapped on the LiDAR and added to the inventory. These added landslides required mapping at a scale below 1:4,000. Landslides originally were not mapped below a scale of 1:4,000 according to the protocol followed in this study (Burns and Madin, 2009).

Of the 153 landslide deposits, 26 are classified as pre-historic (>150 years old). The majority of the landslide deposits (127 landslides) appear to have had movement in the past 150 years. Failures occur on slopes ranging from 12° to 48° with a mean estimated pre-failure slope of 27° ± 8°. Depth to failure surfaces for shallow-seated landslides ranged from 0.75 m to 4.3 m, with an average of 2.9 m ± 0.8 m and depth to failure surfaces for deep-seated landslides ranged from 5 m to 75m, with an average of 18 m ± 14 m. The landslide deposits are highly variable in size. The smallest failure covers

an area of approximately 82 m^2 while the largest deposit covers an area over 1,950,000 m^2.

Earth flows are the most common slope process (110 failures) (Table 8) comprising nearly three quarters (71%) of all mapped deposits in the study area. Of the 110 earth flow deposits, 70 are shallow-seated failures.

Table 8. Number and extent of individual landslide deposits by movement type from landslide inventory.

Landslide Type	Count	Area	Percent Landslide	Percent of Study
		km^2 [mi^2]	Deposits	Area
Complex	21	4.27 [1.65]	14%	16%
Earth Flow	110	3.32 [1.28]	71%	12%
Earth Slide Rotational	6	0.06 [0.02]	4%	0.2%
Debris Flow	15	0.05 [0.02]	10%	0.2%
Earth Slide Translational	1	0.001 [0.0003]	1%	0.004%

While earth flows are the most common failure type, deep-seated, complex landslides cover the highest percentage of the study area (16%). These large, complex deposits occur on moderate, 20° to 35°, slopes with an average mean slope of 26° ± 7°. Depth to failure surfaces ranges from 7 m to 75 m, with an average of 26 m ± 7 m.

The third most common landslide classification is debris flow fan deposits. Debris flow fans were found on slopes ranging from 10° to 30° with estimated fan heights of 1 m to 15 m. Debris flow fan deposits are found on both steep hillsides and shallow gradient valley floors.

Other types of mapped landslides include rotational and translational landslides. The rotational landslides are commonly deep-seated with failure depth surface ranging

from 7 m to 30 m. One historic, shallow-seated translational landslide exists with a failure depth of 4 m.

4.1.2 Landslide Inventory Compared to Previous Studies

The LiDAR-derived landslide inventory map (Figure 15) enhances the detail of previous geologic maps. Wells et al. (1994) mapped seven landslides, covering 5% of the study area. One hundred and fifty three (153) landslides are now mapped, covering 28% of the study area. The locations of the seven landslide deposits are similar between the inventories; however, the landslide margins are variable. While the LiDAR-based inventory was mapped at a scale of 1:4,000, the previous geologic mapping was done at 1:62,500 which could explain some of the discrepancies. A new geologic map was created based upon the LiDAR-based landslide inventory (Figure 16). It now includes the new landslides mapped in addition to the modified landslide boundaries from Wells et al. (1994).

4.2 Mapping Active Landslides with Differential LiDAR

Burns et al. (2010) found a total of 15 active landslides in the December and September, 2007 differential LiDAR dataset (Differential Dataset 1). An example of a debris flow that occurred in this time span and reported in Differential Dataset 1 is shown in Figure 17. The December, 2007 LiDAR was subtracted from the March, 2009 LiDAR to create Differential Dataset 2. A 0.5 m threshold was applied to map active landslides (Figure 18). Probable landslides were mapped based on contiguous positive or negative

elevation change in the down-slope direction or the occurrence of negative elevation change in the upslope direction accompanied with a positive elevation change directly below (Burns et al., 2010). A total of 14 possible active landslides were mapped on Differential Dataset 2. Active landslides were verified at 9 of the 14 sites (Table 9).

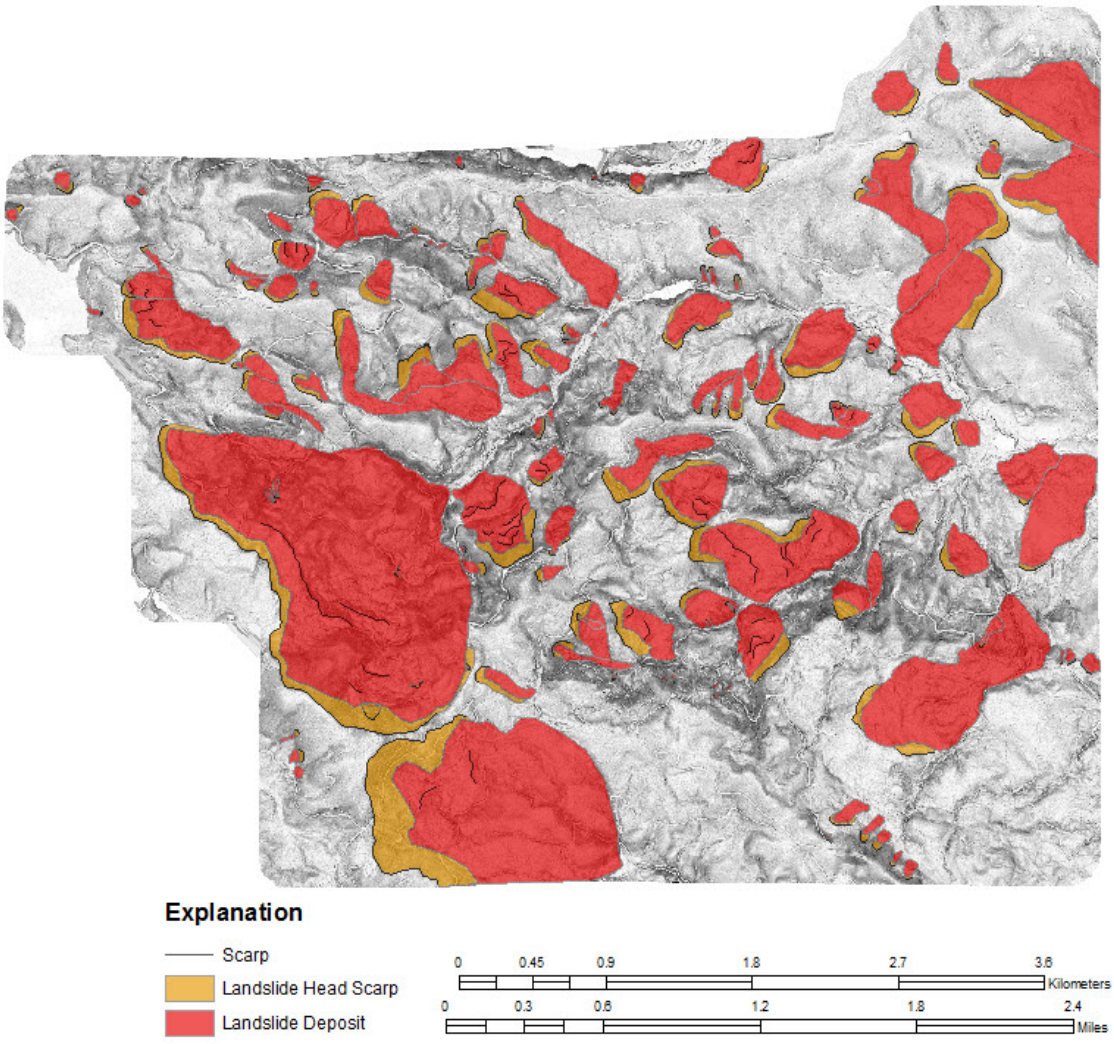

Figure 15. LiDAR-based landslide inventory for the Panther Creek Watershed, Oregon.

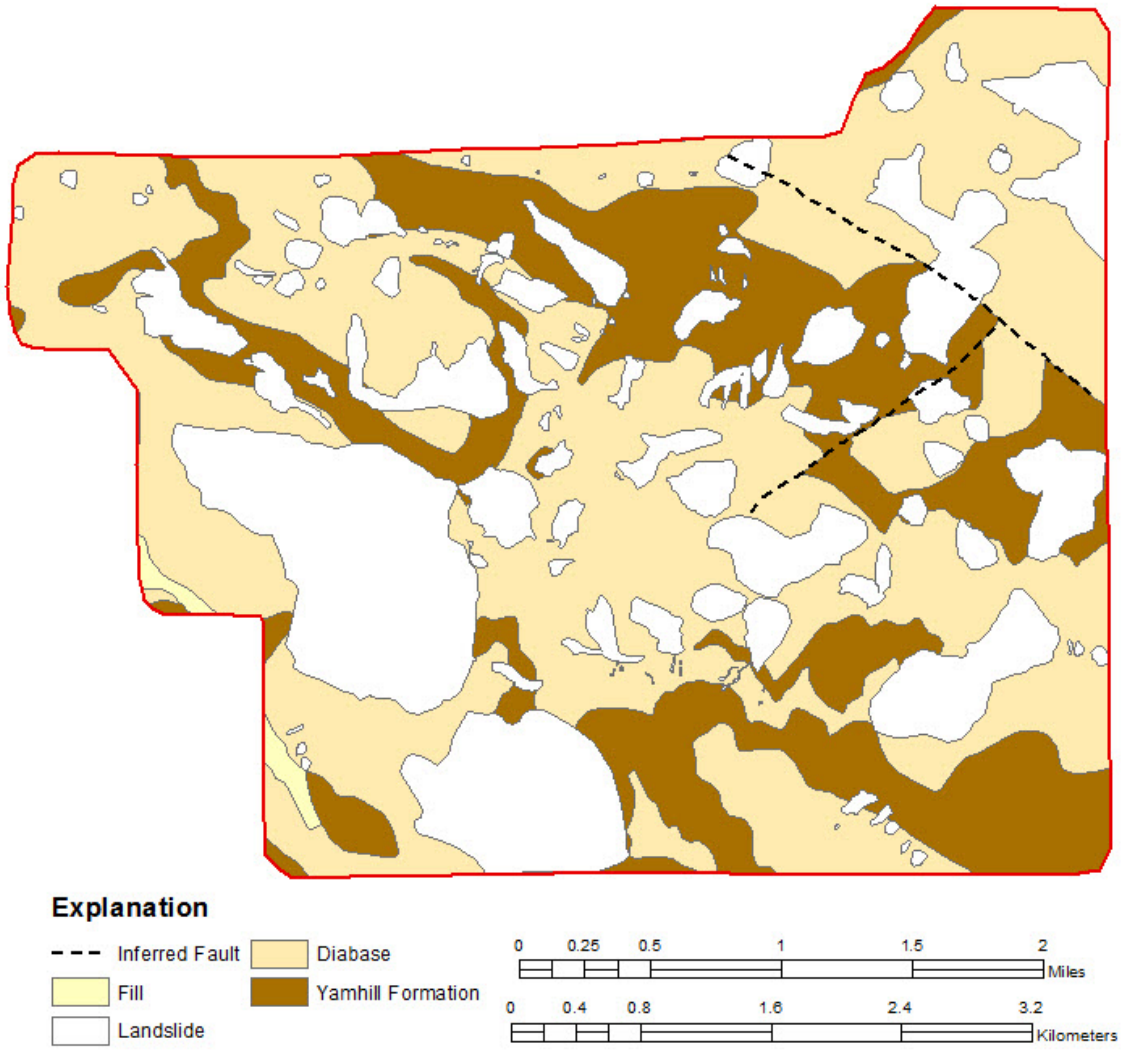

Figure 16. New geologic map modified from Wells et al. (1994) based on LiDAR-based landslide inventory.

Field work conducted in the summer of 2009 resulted in the discovery of several active landslides not found on Differential Dataset 2. A review of Differential Dataset 1, showed that these recent landslides occurred in 2007 increasing the number of recent landslides in Differential Dataset 1 from 15 to 22 (Table 9).

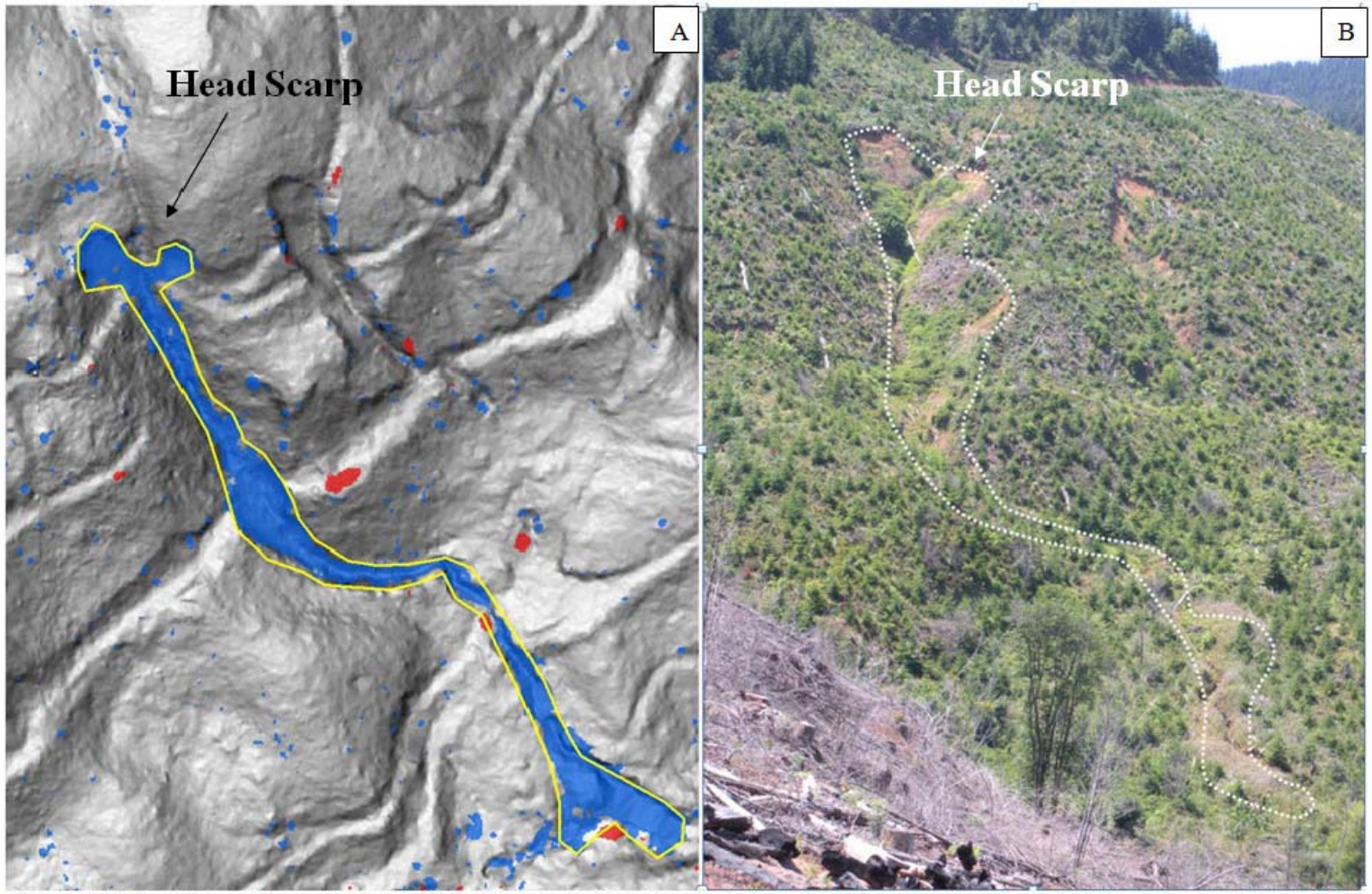

Figure 17. (a) December and September 2007 differential dataset with active debris flow (PC_105) marked in yellow. (b) Field photo of landslide PC_105.

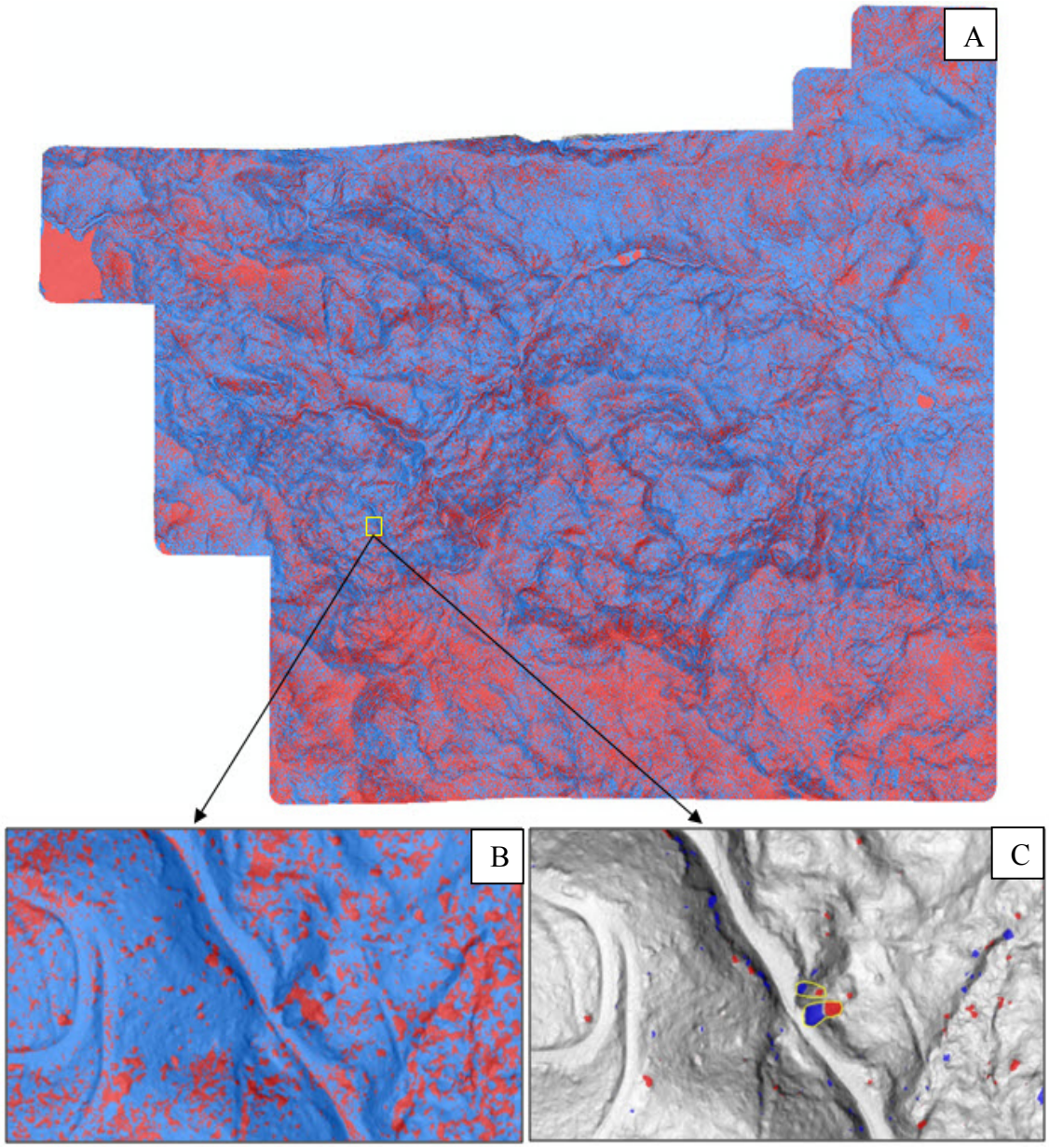

Figure 18. Mapping landslides with differential LiDAR. Blue indicates a decrease in elevation and red indicated an increase in elevation (*a*) Initial subtraction of March 2009 from December 2007 LiDAR. (*b*) Inset of initial subtraction. (*c*) Inset after 0.5 m threshold was applied. Field verified active landslides are marked in yellow.

Table 9. Inventory of recent landslides that occurred in each differential dataset. Landslides that had continued movement in another differential dataset are highlighted in red.

Differential Dataset 1	Differential Dataset 2	Differential Dataset 3
PC_100	PC_50	**PC_156**
PC_101	**PC_103**	
PC_102	**PC_106**	
PC_103	**PC_109**	
PC_104	PC_113	
PC_105	PC_115	
PC_106	**PC_116**	
PC_109	PC_127	
PC_111	**PC_156**	
PC_112		
PC_116		
PC_118		
PC_121		
PC_124		
PC_125		
PC_126		
PC_155		
PC_156		
PC_161		
PC_162		
PC_163		
PC_164		

Of the nine confirmed active landslides in Differential Dataset 2, five of the deposits had initial movement detected in Differential Dataset 1 but also had continued movement in the subsequent differential dataset (Table 9). The March, 1999 landslide that flowed into the Carlton Reservoir had continued movement on a portion of its head scarp. Figure 19 displays landslides that occurred in the same area over the two differential datasets. Two landslides occurred in Differential Dataset 1, PC_115 and PC_118. In Differential Dataset 2, a new landslide occurred (PC_116) and PC_115 also continued to have movement. PC_118, on the other hand, displayed no active movement detected in Differential Dataset 2.

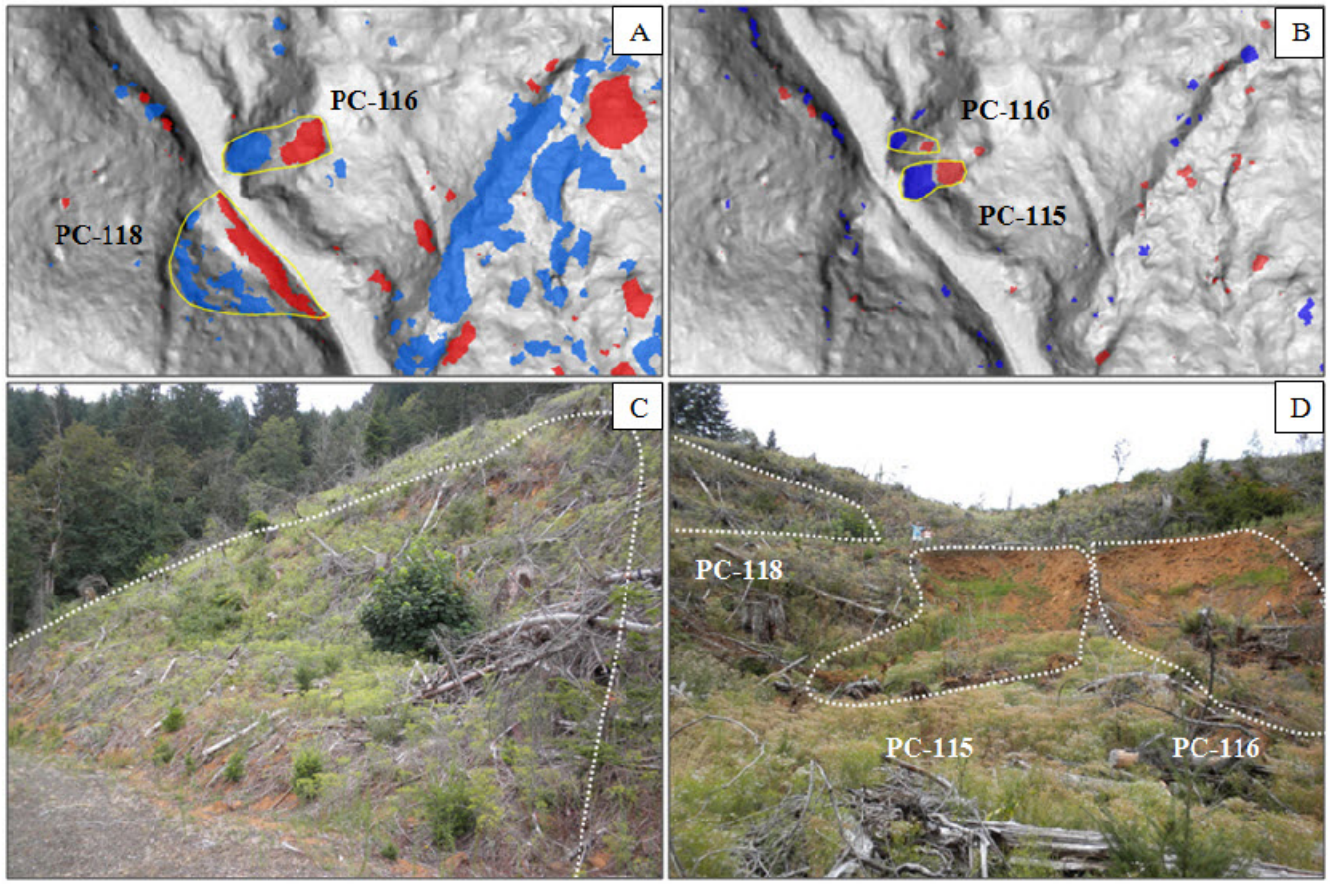

Figure 19. (*a*) December and September 2007 Differential Dataset 1 with active landslides marked in yellow. (*b*) March 2009 and December 2007 Differential Dataset 2 with active landslides marked in yellow at same location as *picture a*. Notice continued movement of landslide PC_116. (*c*) Field photo of landslide PC_118. (*d*) Field photo of landslides PC_115, PC_116, and PC_118.

Differential LiDAR can also be used to track movement of a landslide through time. Landslide PC_156 was originally mapped as a historic landslide deposit based upon its rougher appearance and with well-developed features such as cracks and scarps. The March, 2009 LiDAR was subtracted from the March, 2010 LiDAR to create Differential Dataset 3. Differential Dataset 1, Differential Dataset 2, and Differential Dataset 3 were used to observe current landslide activity at PC_156. Significant movement of the head scarp is detected in Differential Dataset 1 (Figure 20). In the following two differential datasets the head scarp and upper minor scarp had continued movement.

The entire study area was not reviewed for Differential Dataset 3 due to time constraints. Only areas and landslides with previous recent landslide activity were reviewed for further movement. In these areas, no active landslides occurred, except for at the head scarp of PC_156.

Based on the differential inventory and field work, there are 26 active landslides that failed between September, 2007 and March, 2009. The majority of the recent failures are shallow-seated earth flows (Table 10). Only one failure, a rotational landslide, was deep-seated. Failures are occurring on slopes ranging from 20° to 48° with a mean estimated pre-failure slope of 34° ± 8°.

Table 10. Summary of 26 recent landslides that failed between September, 2007 and March, 2009

Landslide Type	Count	Area
		mi^2 [km^2]
Earth Flow	18	0.019 [0.049]
Earth Slide Rotational	2	0.003 [0.007]
Debris Flow	5	0.002 [0.004]
Earth Slide Translational	1	0.0003 [0.001]

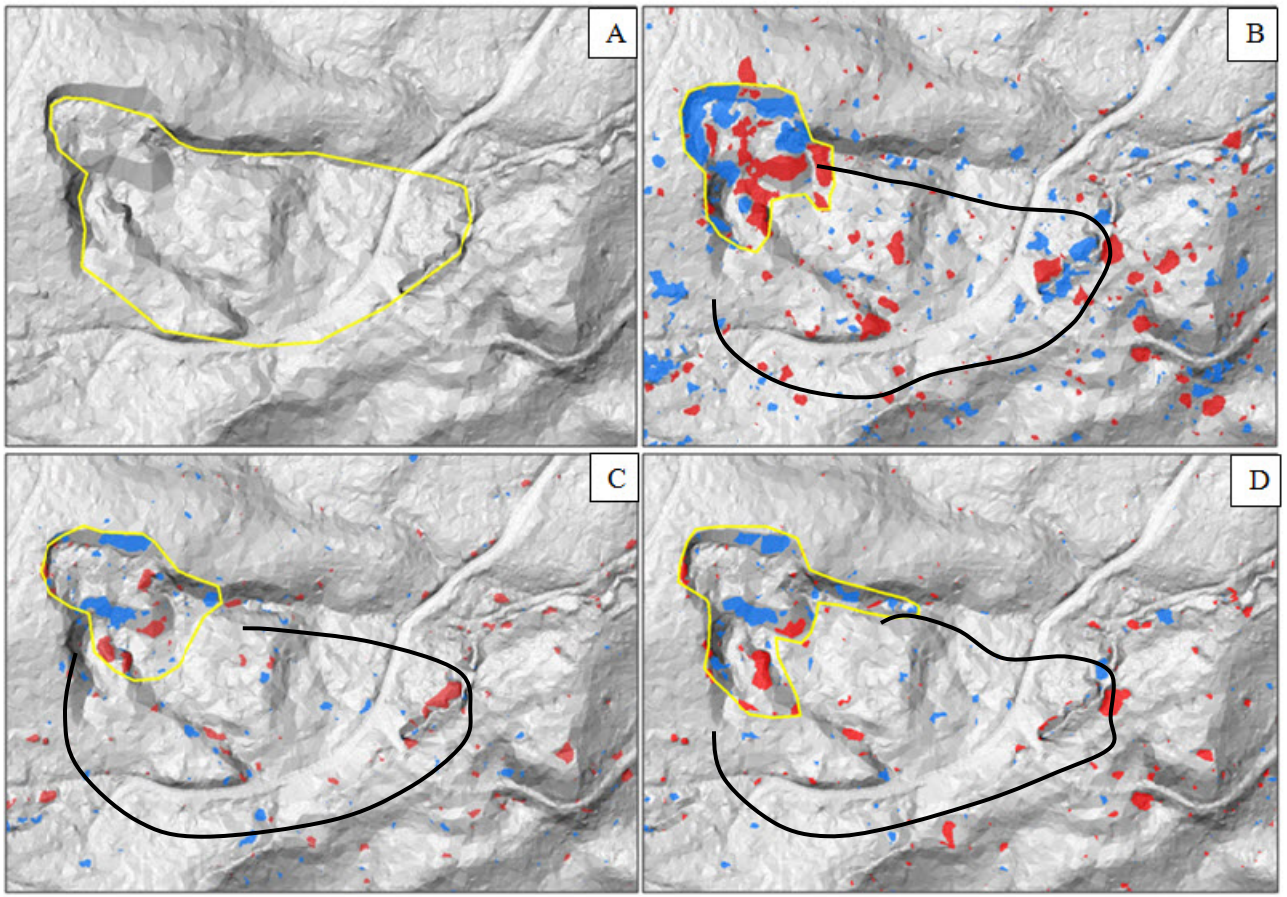

Figure 20. Capturing active movement from one landslide (PC_156) over two differential datasets (*a*) Original mapped historic landslide marked in yellow. (*b*) December and September 2007 Differential Dataset 1 with active extent of landslide movement marked in yellow. (*c*) March 2009 and December 2007 Differential Dataset 2 with active extent of landslide movement marked in yellow. (*d*) March 2010 and March 2009 Differential Dataset 3 with active extent of landslide movement marked in yellow. All show greatest movement at the scarp and toe as mentioned by Burns, 1998a.

4.3 Shallow-Seated Susceptibility Map

The final shallow-seated susceptibility zones (high, moderate, and low) were determined based upon landslide deposit and head scarp locations, calculations of factor of safety, and buffers (Burns et al., In Press). The high susceptibility zone included the landslide deposits, head scarps, head scarp buffers, areas with calculated factor of safety < 1.25. The high susceptibility zone covers 9.6 km^2 or approximately 35% of the study area (Figure 21). The moderate susceptibility zone was created based on areas with calculated factor of safety between ≤ 1.5 and > 1.25 and a 2H:1V buffer around areas with factor of safety calculations <1.5. The moderate susceptibility zone covers 13.5 km^2 or approximately 49% of the study area. Only 16% of the study area has a low potential for shallow-seated landslides. The areas with low potential are commonly flat with low slope angles.

4.4 Deep-Seated Susceptibility Map

The deep-seated susceptibility zones were established based upon locations and proximity to deep-seated landslide deposits and head scarps, head scarp buffers, susceptible geologic units, slope angles, and mapper judgment (Burns, 2008). The high susceptibility zone included the landslide deposits, head scarps, and head scarp buffers. The high susceptibility zone covers 10.5 km^2 or approximately 38% of the study area (Figure 22). The moderate susceptibility zone was mapped based upon proximity to deep-seated landslide weak geologic units, and slope angles > 10°. The moderate

susceptibility zone covers 11.7 km^2 or approximately 43% of the study area. Only 19% of the study area is not susceptible to deep-seated landslides.

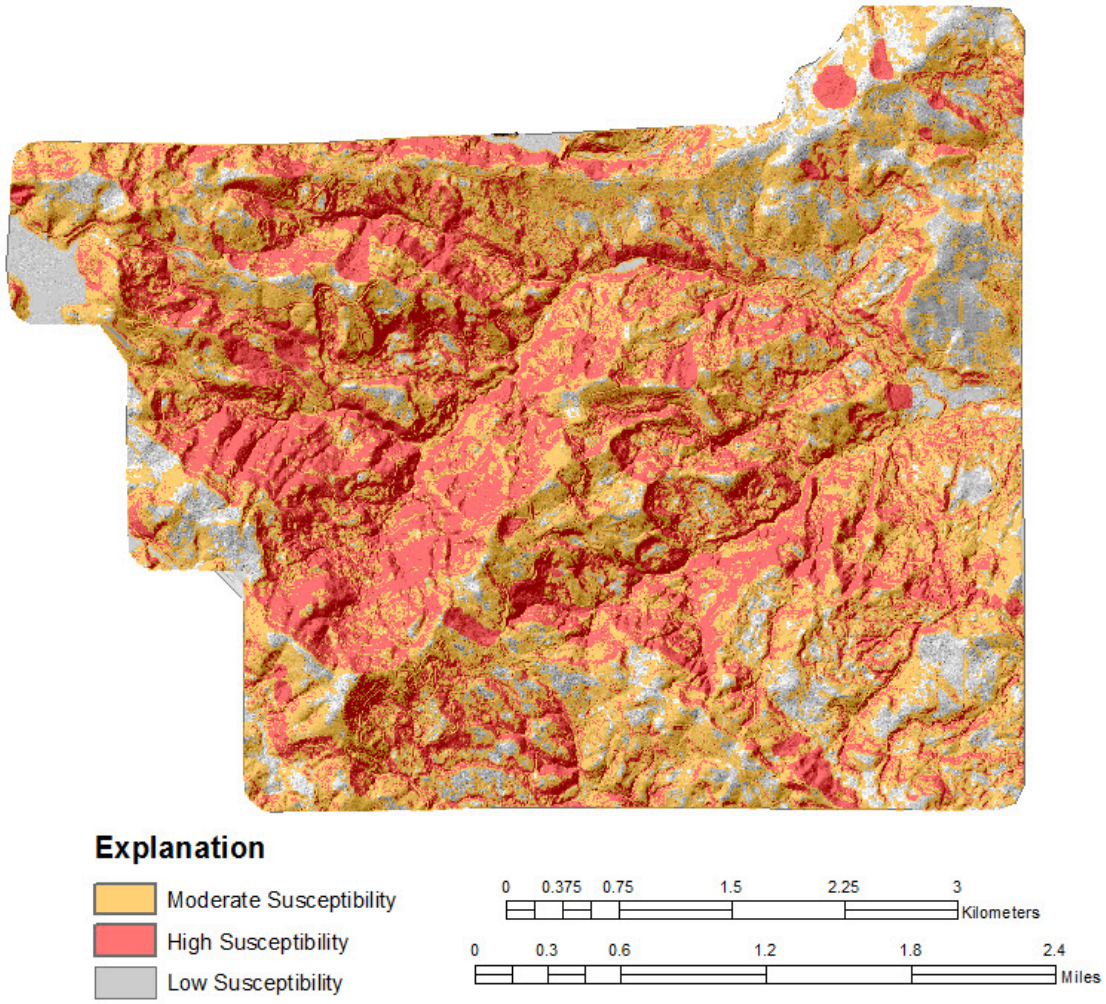

Figure 21. Shallow-seated landslide susceptibility map of the study area displaying high susceptibility in red and moderate susceptibility in orange. Low susceptibility is in gray.

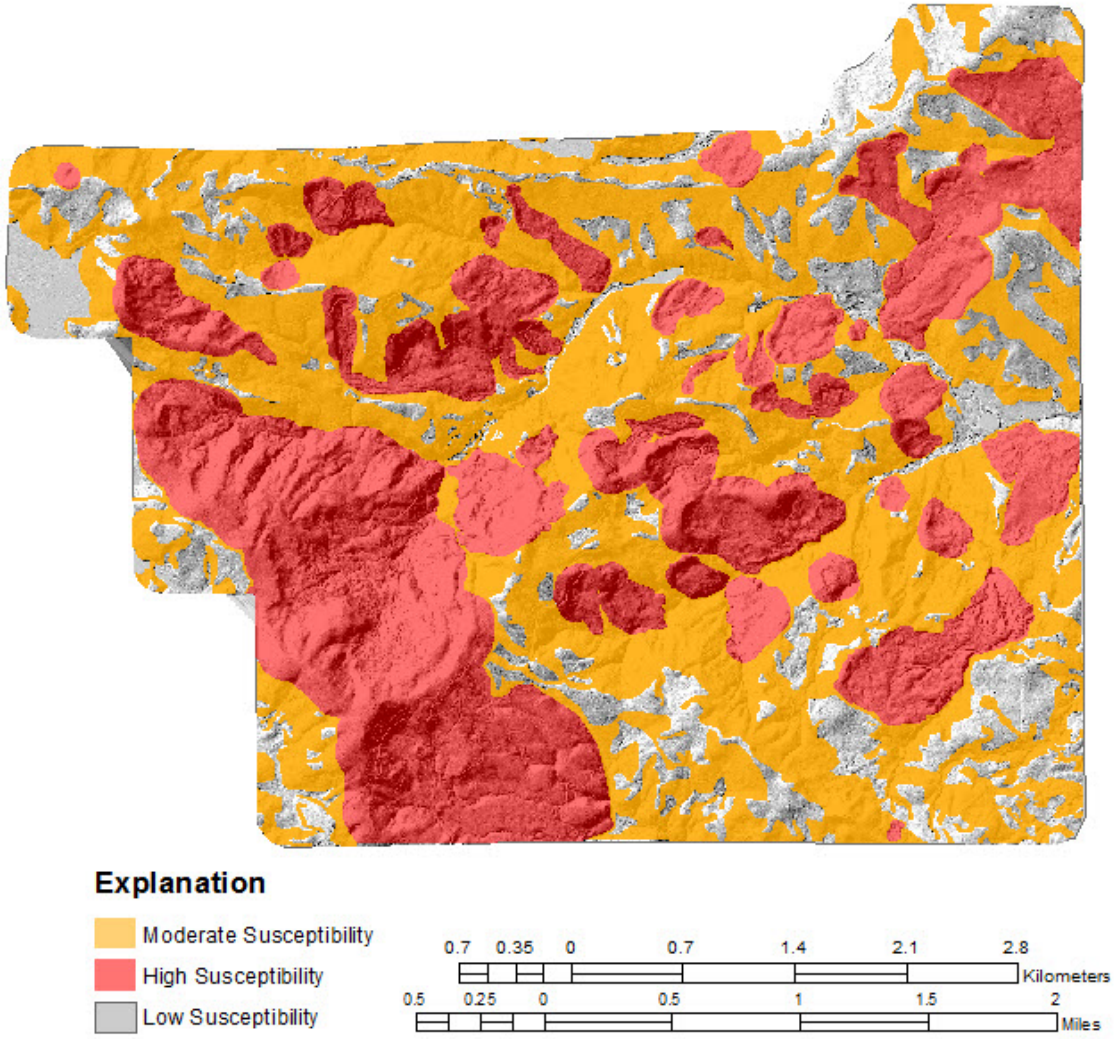

Figure 22. Deep-seated landslide susceptibility map of the study area displaying high susceptibility in red and moderate susceptibility in orange. Low susceptibility is in gray.

Chapter 5: Discussion

5.1 Accuracy of Landslide Mapping on LiDAR

After the landslides were mapped on the LiDAR, 81% of the landslide inventory was field checked. The entire landslide inventory was not field verified due to land access restrictions. Based on field data, 93% of the LiDAR mapped landslides were correctly identified. Nine landslides (7%) were incorrectly identified as landslides on the LiDAR and were removed from the final landslide inventory. The nine misidentified landslides were predominately located in steep drainages. The misidentified landsides ranged in size from 500 - 20,000 m^2. Two of the nine misidentified landslides were borrow pits (areas where material has been dug for use at another location) with an average size of 500 m^2. Based on the high percentage of correctly identified landslides, LiDAR-derived DEMs allow accurate mapping of landslides.

5.2 Factors Controlling Landslide Distribution

The central factor controlling landslide occurrences in the Panther Creek Watershed is the underlying geology. The two dominant geologic units are the mapped diabase (Tidb) and Yamhill Formation (Ty). The majority of landslide failures are occurring in the mapped diabase (Tidb) with 94 separate failures (Table 11). While the bulk of the failures are occurring within this geologic unit, the areal percentage of landslides for the unit is relatively low (16%). The highly-weathered diabase forms thick colluvial layers prone to shallow earth flows.

A total of 22 failures occurred in the siltstone of the Yamhill Formation. These landslides are predominantly earth flows and complex failures. Approximately 60% of the failures are deep-seated in the Yamhill Formation. All of the shallow-seated landslides are earth flows. No failures occurred in the Quaternary alluvial sediments (Qf), however, this geologic unit covers less than 1% of the study area. A total of 37 landslides occur within both the the Yamhill Formation (Ty) and diabase (Tidb).

Table 11. Percent areas of landslide and landslide occurrences for each geologic unit in the study area.

Geologic Unit	% Geologic Unit in study area	% Area of Landslide within Geologic Unit	Number of Landslide Occurrences
Tidb	64	16	94
Ty	30	8	22
Qf	< 1	0	0
Tidb and Ty	-	-	37

5.3 Factors Controlling Recent Landslide Distribution

There are 26 active landslides in the study area since 2007. Half of the new landslides (14 landslides or 54%) are failing in recently clearcut areas (0-5 years old) (Figure 23). Tree stand ages were grouped based on data provided by the Bureau of Land Management (2005). Three of these landslides occurring in recently clearcut areas also occur along a logging road (Figure 24). The recently harvested areas generally have not been replanted. Three other recent landslides failed in past clearcut areas that had been harvested 5-20 years ago. These areas have been replanted and contain little to no canopy but contain thick understory vegetation. Four new landslides failed in recently clearcut areas along roadways; two on logging roads and two on a maintained roadway.

The logging roads are commonly not engineered since they were predominantly built for temporary access to timber management areas. The remaining five recent landslides failed in unmanaged mature growth forest.

Figure 23. Landslide PC_104 that failed between September and December 2007 in a recently clearcut area.

Nine of the recently active landslides failed within the boundaries of older landslide deposits. Three failures occurred on older landslide head scarp terrain and three failures occurred on old landslide toes (Figure 25). Of these nine failures, five occurred within historic landslides (<150 years old).

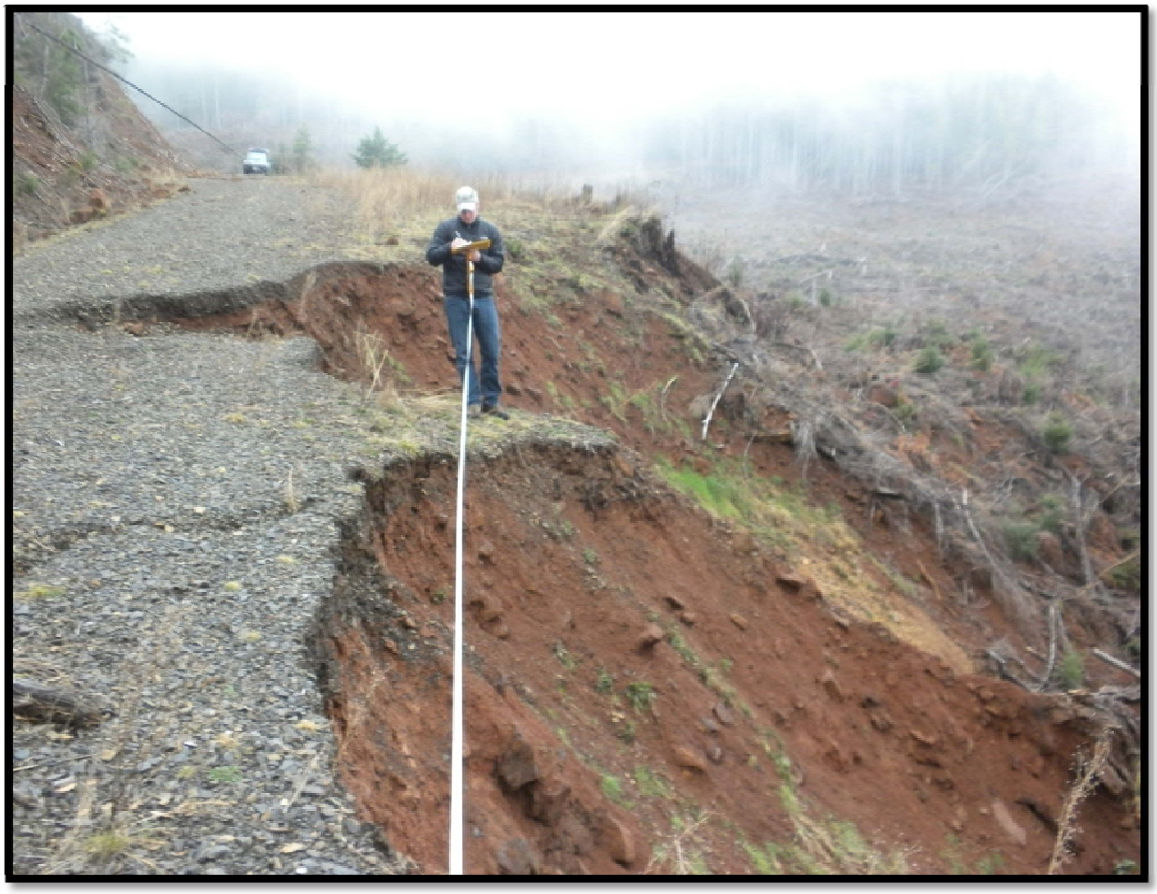

Figure 24. Recent landslides (PC_115 and PC_116) failing along a logging road in a recently harvested area.

5.4 False landslide identification with differential LiDAR

After the December, 2007 was subtracted from the March, 2009 LiDAR, a total of 14 possible active landslides were mapped on Differential Dataset 2. Active landslides were verified at 9 of the 14 sites (64%). All 5 misidentified sites, however, were assigned a low confidence rating prior to field verification. The 9 verified landslides all had a high confidence rating.

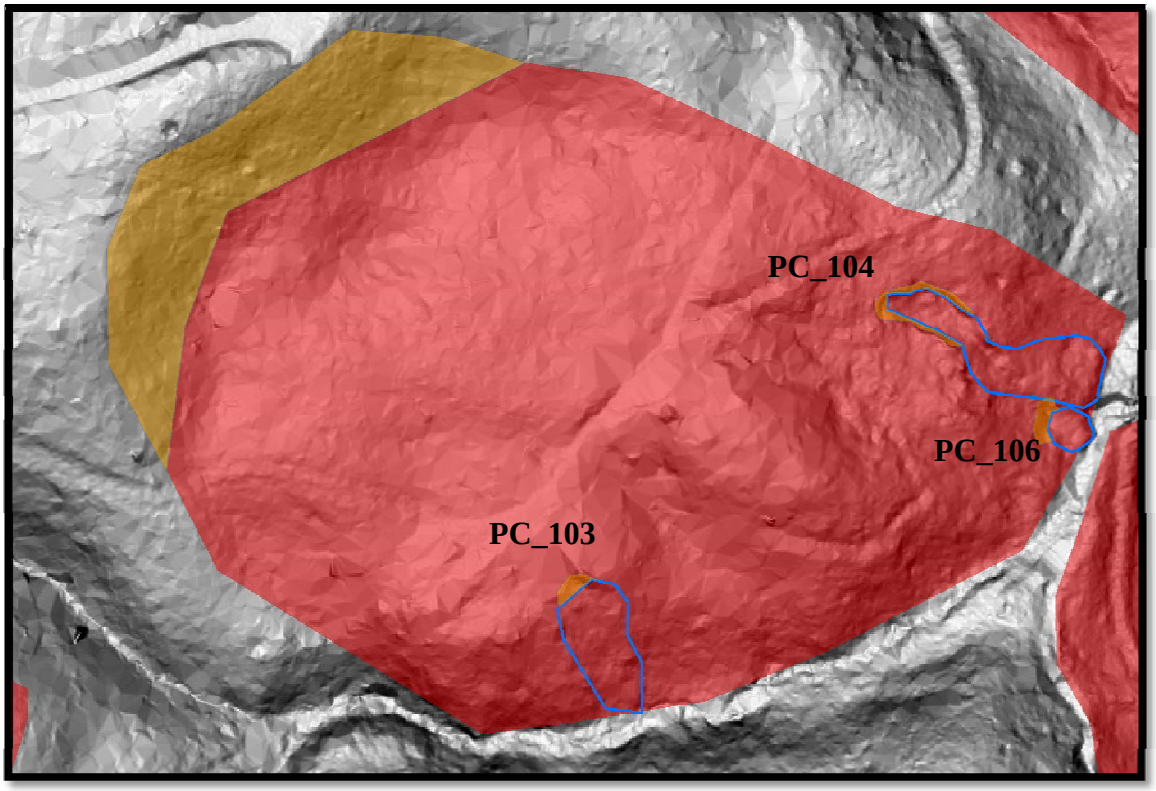

Figure 25. Three recent landslides (outlined in blue) failing on the toe of a historic landslide deposit PC_68 (in red).

Burns et al. (2010) subtracted the September, 2007 from the December, 2007 LiDAR (Differential Dataset 1) and misidentified 13 out of 28 active landslide sites. However, 12 out of the 13 misidentified sites were assigned a low confidence rating. In their study, two thirds of the misidentified landslide sites were in young clearcuts (0-5 years old) and one third were in mature forest areas. They concluded that the presence, age, and type of vegetation affected their capability to correctly identify active landslides.

The five misidentified landslide sites in my study were found along roads, stream channels, and in clearcut and mature forest areas. Two misidentified landslides were found in clearcut areas that had been replanted. These areas have short (4 – 8 m)

Douglas-fir trees and also contain dense vegetation including evergreen shrubbery (Figure 26). Evergreen shrubs, like salal, keep their foliage year round. This short, dense vegetation can cause a reduction in LiDAR point density and can result in what appears to be an elevation change when in fact no actual change in ground elevation has occurred.

The third misidentified landslide was present along an active stream channel. Natural erosion processes from the stream or the thick vegetation surrounding the channel may have led to false identification. Errors in the LiDAR data are common in areas with steep slopes, like the vertical walls of stream banks.

The fourth incorrectly identified landslide was located on a steep area, and a section of the hill had been subjected to a fire causing approximately 1 m (depth) of the brush to burn. This decrease in elevation likely caused to misidentification.

The last incorrectly classified landslide was located in a steep, young forest area along a road. The misidentification could have been caused by erosion from a road cut and a deposit of side-cast fill or the thick, young vegetation (Figure 27).

5.5 Comparing Rainfall Data and the Differential Datasets

During the three months between the LiDAR collection of Differential Dataset 1 (September – December 2007), 72 cm of rainfall (an average of 24 cm/month) was recorded at the dam at Haskins Creek Reservoir (Figure 2) (Figure 28). However, nearly half of this collective rainfall (34 cm) fell during a storm on December 2-4, 2007 (Burns et al., 2010). During this three month period, 22 landslides occurred in the study area. The large number of landslides may have been due to this large storm event in December.

Figure 26. Short, dense vegetation in recently replanted clearcut areas are common in the study area. This type of vegetation can lead to false identification of active landslides when using differential LiDAR.

Figure 27. Misidentified landslide possibly caused by thick, young, deciduous vegetation.

During the fifteen months between the LiDAR collection of Differential Dataset 2 (December 2007 – March 2009), 218 cm of rainfall (an average of 14.5 cm/month) was recorded at the dam (Figure 29). Only one significant storm event occurred during this time period on January 1st, 2009. In a 24 hour period, 12 cm of rainfall was recorded at the dam. Wiley, 2000, found that there is a linear relationship between rainfall intensity and landsliding in western Oregon. For the study area, 7-10 cm of rainfall in a 24 hour period can trigger landslides and debris flows (Wiley, 2000). The 12 cm of rainfall exceeds these threshold values, indicating the slope failures were possible from this storm event. During this 15 month span, however, only four new landslides occurred and five landslides that moved in Differential Dataset 1 had continued movement. The absence of major storm events during the collection of LiDAR for Differential Dataset 2, may have contributed to the lack of landslide movement.

5.6 Accuracy of the Landslide Susceptibility Maps

The shallow-seated susceptibility map was compared to the locations of active landslides that failed between September, 2007 and March, 2009. In order to evaluate the capture rate of the shallow-seated susceptibility map, the map was assessed prior to the addition of all shallow-seated landslide deposits. There are 19 active shallow-seated landslides in the study area. These 19 deposits were examined in two ways: 1) an aggregated area of all of the landslide polygons and 2) each individual landslide polygons (Burns et al., In Press). 97% of the aggregated active landslide inventory was captured within the moderate or high susceptibility zone.

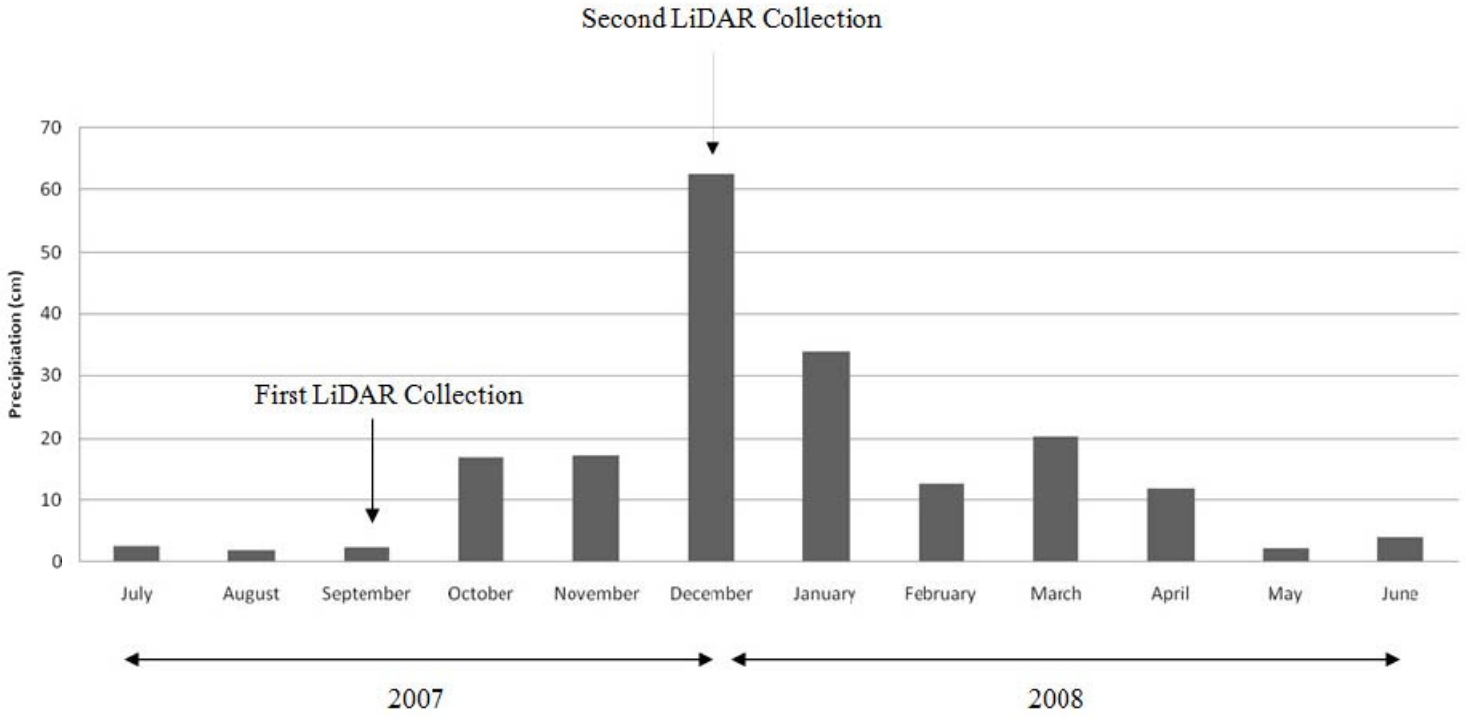

Figure 28. Graph of precipitation between the LiDAR data collection for Differential Dataset 1.

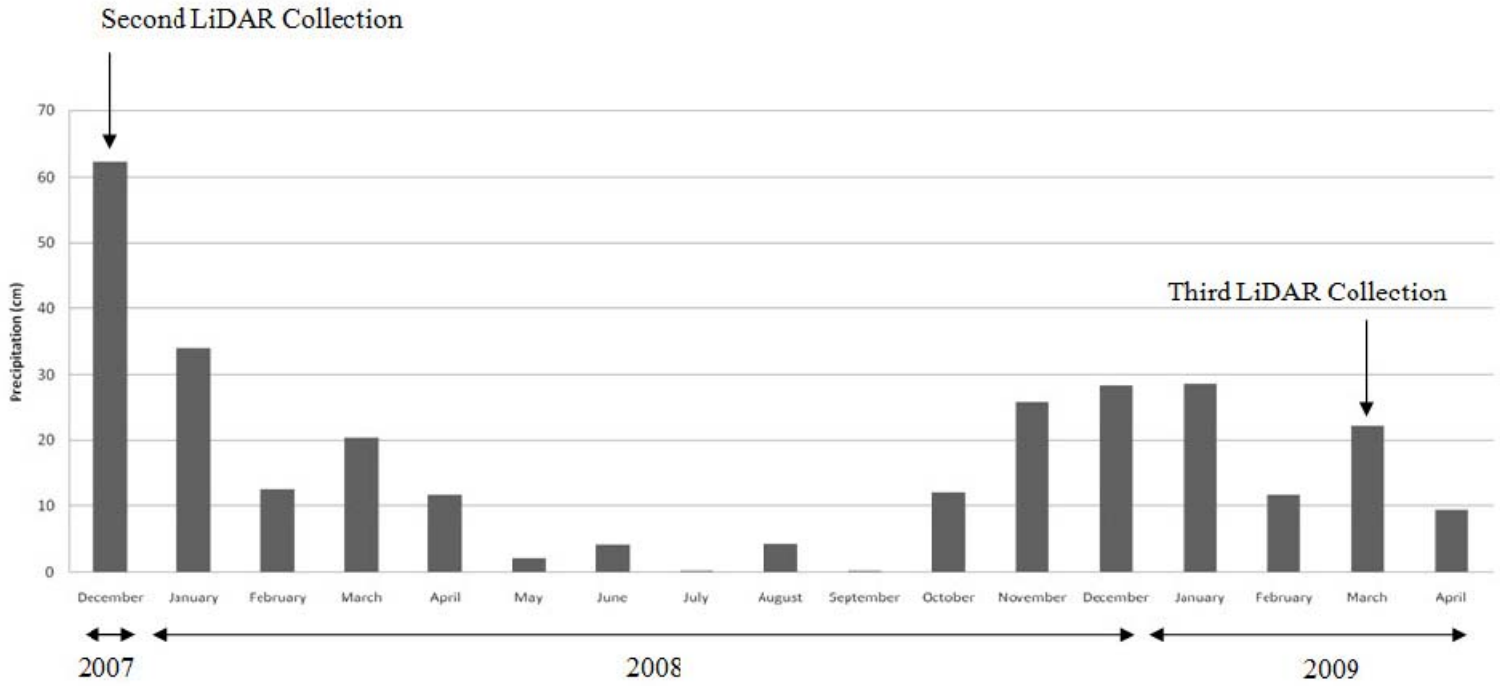

Figure 29. Graph of precipitation between the LiDAR data collection for Differential Dataset 2

Next, the shallow-seated susceptibility map was evaluated for each individual landslide polygon. Percent captured was based upon if each individual landslide polygon touched the high or moderated zone with a minimum of 9 grid cells. 99.9% of each individual landslide polygons touched (minimum of 9 grid cells) the moderate or high susceptibility zone.

The deep-seated susceptibility map was compared to the locations of active landslides, however, only part of one of the deep-seated landslide failed between September, 2007 and March, 2009. The high susceptibility zone includes the deep-seated landslides and head scarps locations and head scarp buffer. Since the new deep-seated landslide is a reactivation of the upper head scarp and minor scarp of a historic landslide, it was captured 100% in the high susceptibility zone. Large, deep-seated landslides can move over time and reactivation often is focused upslope near the landslide head scarp and at the landslide toe (Burns, 1998b).

Chapter 6: Conclusions

The March, 2009 LiDAR-derived bare-earth digital elevation models (DEMs) were used to locate and map landslide deposits, flanks, head scarps, and minor scarps in the Panther Creek Watershed of the Oregon Coast Range following protocol developed by Burns and Madin (2009). A landslide geodatabase (Appendix B) was created to describe each landslide deposit as to type of movement (slide, flow, spread, topple, fall, or complex) and type of material (rock, earth, debris). Other attributes including head scarp height, estimated failure depth, estimated age, area and volume were also recorded. A total of 153 landslides were mapped on the LiDAR in the 27 km^2 watershed and 81% of mapped deposits were field checked in the summer of 2009. Based on field data, 93% of the LiDAR mapped landslides were correctly identified.

Earth flows are the most common slope processes, comprising nearly three quarters (110 or 71%) of all mapped deposits in the study area. Deep-seated complex landslides (21 total) cover the highest percentage of the study area (16%). The other landslides were classified as debris flows (14 total) or rotational slides (6 total). Only one translational landslide is present in the study area.

Of the 153 landslide deposits, 26 are classified as pre-historic (>150 years old) and 127 landslides appear to have had movement in the past 150 years. Failures occur on slopes ranging from 12° to 48° with a mean estimated pre-failure slope of 27° ± 8°. Depth to failure surfaces for shallow-seated landslides ranged from 0.75 m to 4.3 m, with an average of 2.9 m ± 0.8 m and depth to failure surfaces for deep-seated landslides

ranged from 5 m to 75m, with an average of 18 m ± 14 m. The smallest failure covers an area of approximately 82 m^2 while the largest deposit covers an area over 1,950,000 m^2.

The use of LiDAR resulted in the identification of 21 times the number of landslides previously mapped in the study area. Wells et al. (1994) originally mapped only seven landslides, covering 5% of the study area. One hundred and fifty three (153) landslides are now mapped, covering 28% of the study area. Mapping with LiDAR has not only increased the number of landslides identified, but also improved the accuracy of the spatial extent of the previously mapped landslides.

Recently active landslides were mapped using differential LiDAR. The December, 2007 was subtracted from the March, 2009 LiDAR (Differential Dataset 2) and a total of 14 probable active landslides were mapped on the differential dataset. Active landslides were verified at 9 of the 14 sites, however, the 5 misidentified sites had been assigned a low confidence prior to field verification. The misidentified sites were found along roads, stream channels, and in clearcut and mature forest areas. Steep slopes, young, thick vegetation, and vegetation with foliage year round reduces LiDAR point density and can result in what appears to be an elevation change when in fact no actual change in ground elevation has occurred.

The presence, age, and type of vegetation affect the ability to correctly identify active landslides; therefore it is recommended that LiDAR be collected during leaf-off conditions to map recent landslides. After subtracting the LiDAR datasets, a threshold must be applied to the data to eliminate elevation overestimation. The 0.5 m threshold used is applicable to forested areas in Pacific Northwest; however, this threshold value

may be adjusted based on the topography and geography of an area. The mapped probable landslides must be field checked in order to verify actual active landslide activity. The application of differential LiDAR to map active landslides is best utilized after a major storm event.

Based on the differential inventory and field work, there are 26 active landslides that failed between September, 2007 and March, 2009. The majority of the active failures are shallow-seated earth flows. Only one failure, a rotational landslide, was deep-seated. Half of the active landslides (14 landslides or 54%) are failing in recently clearcut areas. Nine of the recently active landslides also failed within the boundaries of older landslide deposits.

A shallow-seated susceptibility map was created based upon landslide deposit and head scarp locations, calculations of factor of safety, and buffers (Burns et al., In Press). The high susceptibility zone covers 9.6 km^2 or approximately 35% of the study area and the moderate susceptibility zone covers 13.5 km^2 or approximately 49% of the study area. Only 16% of the study area is in the low susceptibility zone.

The accuracy of the shallow-seated susceptibility map was judged according to the locations of active landslides that failed between September, 2007 and March, 2009. 97% of the aggregated active landslide deposits were captured within the high or moderate susceptibility zone and 99.9% of each individual deposit touched (with at least 9 grid cells) the high of moderate susceptibility zone. The shallow-seated susceptibility map is therefore successful at capturing the locations of the recent deposits.

A deep-seated susceptibility map was created based upon locations and proximity to deep-seated landslide deposits and head scarps, head scarp buffers, geologic units, slope angles, and mapper judgment (Burns, 2008). The high susceptibility zone covers 10.5 km^2 or approximately 38%, and the moderate susceptibility zone covers 11.7 km^2 or approximately 43% of the study area. Only 19% of the study area has a low potential for deep-seated landslides.

The accuracy of the deep-seated susceptibility map was judged according to the locations of active landslides in the study area, however, only one deep-seated landslide failed between September, 2007 and March, 2009. The one recent deep-seated landslide falls 100% in the high susceptibility zone. More work will have to be done in order to access the accuracy of this deep-seated susceptibility map.

The methods presented in this thesis can be applied to other areas in Oregon. Differential LiDAR may be used to monitor active landslides and to assess the spatial distribution of landslide occurrences over specific time periods. Shallow- and deep-seated susceptibility maps will help communities to identify areas prone to future landslides. These susceptibility maps can be used to guide and plan regional investigations for future developments. Future developments may include expansion of the reservoirs; however, major infrastructure developments are not planned in this area. Based on the high number of landslides present, the recent landslide activity, and the high percentage of area susceptible to landsliding, the Panther Creek Watershed will continue to have landslide problems in the future.

Chapter 7: Future Work

Due to time constraints, the March, 2010 LiDAR was not thoroughly analyzed in this study. The March, 2009 LiDAR was subtracted from the March, 2010 LiDAR to create Differential Dataset 3, however, only areas with previous recent landslide activity were reviewed for further movement. Differential LiDAR should be employed to map active landslides between March, 2009 and March, 2010 throughout the entire study area. After the recent failures have been mapped, their locations and the factors controlling them should be compared to the failures mapped in Differential Datasets 1 and 2. Future LiDAR acquisitions have also been commissioned for 2011- 2013. Differential landslide mapping should also be included on these LiDAR datasets.

The use of threshold values with differential LiDAR to eliminate ground change overestimation should be further explored. Vegetation in the field area is not consistent throughout. Vegetation plots range from areas with no vegetation (recent clearcuts) to areas with young, thick vegetation, to mature growth forest. The root mean square errors (RMSE) will vary based on the height and type of vegetation (Burns et al., 2010). Based on the inconsistent vegetation and therefore varying RMSE values, the use of a single threshold value to eliminate ground change overestimation may not be applicable. Different threshold values should be tested on each vegetation plot type to elucidate which values work best based upon the type of vegetation. The use of several different threshold values may increase the mapper's ability to correctly identify active landslides in this study area.

The creation of susceptibility maps were discussed in detail in this thesis. The next type of susceptibility map to be created should be a debris flow susceptibility map. While debris flows accounted for only 10% of the total inventory, there potential impacts to people, infrastructure, and water quality are vast. Therefore, the location of future debris flows should be explored in the future.

Future work should also include the creation of a risk map. A landslide risk map combines landslide susceptibility with an analysis of expected consequences (infrastructure damage and loss of life) from landslide damage. The study area is remote, with few residents and infrastructure, however, three reservoirs supply drinking water for the cities of Carlton and McMinnville. Risk to these reservoirs should be evaluated.

References

Ardizzone, F., Cardinali, M., Galli, M., Guzzetti, F., and Reichenbach, P., 2007, Identification and mapping of recent rainfall-induced landslides using elevation data collected by airborne Lidar: Natural Hazard and Earth System Sciences, v. 7, p. 637-650.

Bureau of Land Management, 2005, Forest Cover/Operations Inventory Publication Version GIS Database: U.S. Department of the Interior, Bureau of Land Management, Tillamook, Oregon.

Burns, S. F., 1998a, Landslide Hazards in Oregon, *in* Burns, S. F., ed., Environmental, Groundwater, and Engineering Geology: Applications from Oregon: Belmont, California, Star Publishing, p. 303-315.

Burns, S. F., 1998b, Landslides in the Portland Area Resulting from the Storm of February, 1996, *in* Burns, S. F., ed., Environmental, Groundwater, and Engineering Geology: Applications from Oregon: Belmont, California, Star Publishing, p. 353-365.

Burns, S.F., Burns, W.J., James, D., and Hinkle, J., 1998, Landslides in the Portland, Oregon Metropolitan Area Resulting from the Storms of February, 1996: Inventory Map, Database and Evaluation, METRO, Portland, Oregon, 41 p.

Burns, W.J., 1999, Engineering geology and relative stability of the southern half of Newell Creek Canyon, Oregon City, Oregon: Portland State University, Department of Geology, M.S. Thesis, 143 p., 3 plates.

Burns, W.J. and Madin, I.P., 2006, Mapping Portland Landslides with LIDAR: Department of Geology and Mineral Industries Cascadia, vol. 4, no. 2, pp.6-7.

Burns, W.J., 2007, Comparison of remote sensing datasets for the establishment of a landslide mapping protocol in Oregon. AEG Special Publication 23: Vail, Colo., Conference Presentations, 1st North American Landslide Conference.

Burns, W.J., Madin, I.P., Ma, L., 2008, Statewide landslide information layer for Oregon (SLIDO), release 1: Department of Geology and Mineral Industries Digital Data Series SLIDO-1, 45p., 1 pl.

Burns, W.J., 2008, Regional Landslide Hazard Maps of the Southwest Quarter of the Beaverton Quadrangle, West Bull Mountain Planning Area, Washington County, Oregon: Department of Geology and Mineral Industries, Open-File Report O-08-09 21 pp.

Burns, W.J., Madin, I.P., 2009, Protocol for inventory mapping of landslide deposits from light detection and ranging (lidar) imagery: Department of Geology and Mineral Industries Special Paper 42, 34 pp.

Burns, W.J., Coe, J.A., Kaya, B.S., and Ma, L., 2010, Analysis of elevation changes detected from multi-temporal LiDAR surveys in forested landslide terrain in western Oregon, Environmental & Engineering Geoscience, v. 16, no. 4, p. 315-341.

Burns, W.J., Madin, I.P., and Mickelson, K.A., In Press, Protocol for shallow-landslide susceptibility mapping: Oregon Department of Geology and Mineral Industries Special Paper 43.

Burns, W.J. and Mickelson, K.A., 2010a. Landslide Inventory Maps for the Astoria Quadrangle, Clatsop, County, Oregon, Oregon Department of Geology and Mineral Industries, IMS-31, Plates 1, 2, 3, 4.

Burns, W.J. and Mickelson, K.A., 2010b. Landslide Inventory Maps for the Oregon City Quadrangle, Clackamas, County, Oregon, Oregon Department of Geology and Mineral Industries, IMS-30, Plates 1, 2, 3.

Burns, W.J. and Mickelson, K.A., In Press. Landslide Inventory Maps for the Silverton Quadrangle, Marion County, Oregon, Oregon Department of Geology and Mineral Industries.

Cornforth, D.H., 2005, Landslides in Practice: Investigation, Analysis, and Remedial/Preventative Options in Soils: Hoboken, New Jersey, John Wiley and Sons, Inc. p. 596.

Cruden, D. M. and Varnes, D. J., 1996, Landslides types and processes, *in* Turner, A. K. and Schuster, R. L. (Editors), Landslides: Investigation and Mitigation: Transportation Research Board, Special Report, v. 247, pp. 36-75.

Hoffert-Hay, D., 2001, North Yamhill Watershed Assessment: Yamhill Basin Council, McMinnville, Oregon: http://www.co.yamhill.or.us/ybc/asmtNY.htm.

Hofmeister, R.J., 2000, Slope failures in Oregon: GIS inventory for three 1996/97 storm events: Oregon Department of Geology and Mineral Industries, Special Paper 34, 20.

McFadden, G., 2010, Panther Creek LiDAR Technical Workshop, Personal Communication: Corvallis, Or.

McKean, J. and Roering, R., 2004, Objective landslide detection and surface morphology mapping using high-resolution airborne laser altimetry: Geomorphology, v. 57. P. 331-351.

Oregon Residential Specialty Code, R404.5, 2008

Orr, E.L. and Orr W.N., 1999, The geology of Oregon: Iowa, Kendall/Hunt Publishing Company, 254 p.

Otte, G.E, Setness, D.K., Anderson, W.A., Herbert, F.J., and Knezevich, C.A., 1974, Soil Survey of Yamhill Area, Oregon: Soil Conservation Service, 90 p., Washington, D.C.

Pointer, S., 1999, "Carlton's water woes get worse: water treatment plant choked with silt unable to keep up with demand": News Register/McMinnville Oregon.

Roering, J. J., Kirchner, J. W., and Dietrich, W. E., 2005, Characterizing structural and lithologic controls on deep-seated landsliding: Implications for topographic relief and landscape evolution in the Oregon Coast Range, USA: Bulletin of the Geological Society of America, v. 117, no. 5-6, p. 654-668.

Schultz, W.H., 2004, Landslides mapped using LIDAR imagery, Seattle, Washington: United States Geological Survey, Open-File Report 2004-1396 pp. 1-11.

Sidle, R.C. and Ochiai, H., 2006, Landslides: Processes, Prediction, and Land Use, Water Resources Monograph 18: Washington D.C., American Geophysical Union, 312 p.

Snavely, P.D., Jr., McLeod, N.S., and Rau, W.W., 1969, Geology of the Newport area, Oregon: The Ore Bin, v. 31, p. 25-71.

Theule, W.J., 2009, Determining Landslide Susceptibility along Natural Gas Pipelines in Northwest Oregon: Portland State University, Department of Geology, M.S. Thesis, 269 p.

USDA-NRCS Official Soil Series Description Query Facility (2009) http://ortho.ftw.nrcs.usda.gov.

Van Westen, C.J. and Getahun, F., 2003, Analyzing the evolution of the Tessina Landslide using aerial photographs and digital elevation models: Geomorphology, v.54, p. 77-89.

Watershed Sciences Inc., 2008, LiDAR Remote Sensing Data Collection: Yamhill County, Oregon.

Wells, R. E., Snavely, P. D. Jr., Macleod, N. S., Kelly, M. M., and Parker, M. J., 1994, Geologic Map of the Tillamook Highlands, Northwest Oregon Coast Range: U. S. Geological Survey Open-File Report 94-21, 23p. and two oversize sheets, scale 1:62,500.

Wheeler, K. L., Wells, R. E., Minervini, J. M., and Block, J. L., 2009, Geologic Map of the Carlton Quadrangle, Yamhill County, Oregon: U.S. Geological Survey Open-File Report 2009-1172, scale 1:24,000 and database.

Wiley, T.J., 2000, Relationship between rainfall and debris flowsin western Oregon: Oregon Geology, v. 62, no. 2, p. 25-48.

Worrel, D.W., 1999, Carlton Reservoir Landslide: A Soil and Water Quality Evaluation: Bureau of Land Management, Tillamook, Oregon, 15 p.

Appendix A: Panther Creek Landslide Geodatabase

Unique_ID	Movement Class	Confidence	Age	Date Last Move	Geology	Slope (°)	Scarp_Height (m)	Fan_Height (m)	Fail_Depth (m)	Deep_Shal	Direction (°)	Area (m^2)	Volume (m^3)
PC_1	Complex-Earth Slide-Rotational+Earth Flow	Moderate (11-29)	Historic (<150yrs)		Tidb, Ty	25	25	10	9.1	Deep	43	90	40213
PC_2	Earth Flow	Moderate (11-29)	Historic (<150yrs)		Tidb	15	6	0	4.0	Shallow	360	20788	120456
PC_3	Earth Flow	Moderate (11-29)	Pre-Historic (>150yrs)		Tidb	20	20	0	18.8	Deep	135	234500	4405660
PC_4	Earth Flow	Moderate (11-29)	Historic (<150yrs)		Tidb	30	9	0	3.0	Shallow	45	4269	33249
PC_5	Earth Flow	High (=>30)	Pre-Historic (>150yrs)		Tidb	20	18	0	16.9	Deep	90	195232	3301130
PC_6	Earth Flow	Moderate (11-29)	Historic (<150yrs)		Tidb	20	8	0	2.0	Shallow	180	1438	10806
PC_7	Earth Flow	Moderate (11-29)	Pre-Historic (>150yrs)		Tidb	32	8	0	6.8	Deep	22.5	15051	102017
PC_9	Earth Flow	Moderate (11-29)	Pre-Historic (>150yrs)		Tidb	20	12	0	11.3	Deep	157.5	140910	1588400
PC_10	Earth Flow	Moderate (11-29)	Historic (<150yrs)		Tidb	12	9	0	3.0	Shallow	157.5	6674	58748
PC_11	Complex-Earth Slide-Rotational+Earth Flow	High (=>30)	Pre-Historic (>150yrs)		Tidb	25	12	0	10.9	Deep	337.5	71388	775971
PC_13	Earth Flow	Moderate (11-29)	Historic (<150yrs)		Tidb, Ty	35	35	12	3.5	Shallow	0	23	7087
PC_14	Earth Flow	High (=>30)	Historic (<150yrs)		Tidb	40	4	0	3.1	Shallow	360	264	809
PC_15	Earth Flow	High (=>30)	Pre-Historic (>150yrs)		Ty	20	8	0	7.5	Deep	135	120802	907825
PC_16	Earth Flow	Moderate (11-29)	Historic (<150yrs)		Ty	25	10	0	9.1	Deep	202.5	12954	117340
PC_17	Earth Flow	Moderate (11-29)	Historic (<150yrs)		Ty, Tidb	35	35	16	2.0	Shallow	0	158	3961
PC_18	Earth Flow	High (=>30)	Historic (<150yrs)		Tidb, Ty	25	25	10	4.0	Shallow	0	23	11970
PC_20	Earth Flow	Moderate (11-29)	Historic (<150yrs)		Ty, Tidb	35	35	8	3.0	Shallow	0	180	1435
PC_21	Earth Flow	Moderate (11-29)	Historic (<150yrs)		Ty, Tidb	18	18	14	13.3	Deep	0	180	40431
PC_22	Earth Flow	Moderate (11-29)	Pre-Historic (>150yrs)		Tidb	20	15	0	14.1	Deep	157.5	64029	902209
PC_23	Complex-Earth Slide-Rotational+Earth Flow	High (=>30)	Historic (<150yrs)		Tidb	32	15	0	12.7	Deep	135	31064	394789
PC_24	Earth Flow	Moderate (11-29)	Historic (<150yrs)		Tidb	25	12	0	4.0	Shallow	22.5	27800	302178
PC_25	Earth Flow	Low (=<10)	Historic (<150yrs)		Tidb	30	3	0	2.6	Shallow	135	8545	22182
PC_26	Earth Flow	Moderate (11-29)	Historic (<150yrs)		Tidb	32	16	0	3.0	Shallow	22.5	5441	73759
PC_27	Earth Flow	Moderate (11-29)	Historic (<150yrs)		Tidb	15	8	0	3.5	Shallow	112.5	8537	65958
PC_28	Earth Slide-Rotational	Moderate (11-29)	Historic (<150yrs)		Tidb	26	10	0	3.0	Shallow	45	4676	42006
PC_29	Earth Flow	High (=>30)	Historic (<150yrs)		Tidb	30	12	0	2.5	Shallow	360	2459	25531
PC_30	Earth Flow	Low (=<10)	Pre-Historic (>150yrs)		Tidb	25	10	0	9.1	Deep	45	20351	184343
PC_31	Earth Flow	Moderate (11-29)	Historic (<150yrs)		Tidb	15	6	0	4.0	Shallow	315	47300	274081
PC_32	Earth Flow	High (=>30)	Historic (<150yrs)		Tidb	25	4	0	3.6	Shallow	45	5037	18251
PC_33	Earth Flow	Moderate (11-29)	Historic (<150yrs)		Tidb	30	4	0	3.5	Shallow	67.5	1324	4581
PC_34	Earth Slide-Rotational	Moderate (11-29)	Historic (<150yrs)		Tidb	30	16	0	13.8	Deep	337.5	8403	116343
PC_35	Complex-Earth Slide-Rotational+Earth Flow	Moderate (11-29)	Pre-Historic (>150yrs)		Tidb, Ty	25	25	25	22.6	Deep	70	45	144523
PC_36	Earth Flow	Moderate (11-29)	Historic (<150yrs)		Ty	25	10	0	4.0	Shallow	90	13689	123993
PC_37	Earth Flow	Moderate (11-29)	Historic (<150yrs)		Ty	15	8	0	7.7	Deep	135	20157	155733
PC_38	Earth Flow	High (=>30)	Historic (<150yrs)		Ty, Tidb	18	18	15	4.0	Shallow	0	135	43365
PC_40	Earth Flow	Moderate (11-29)	Historic (<150yrs)		Tidb	30	10	0	4.0	Shallow	22.5	7254	62773
PC_41	Complex-Earth Slide-Rotational+Earth Flow	Moderate (11-29)	Historic (<150yrs)		Tidb, Ty	30	30	50	43.3	Deep	25	45	62409
PC_42	Earth Flow	High (=>30)	Historic (<150yrs)		Tidb, Ty	15	15	25	24.1	Deep	0	158	175216
PC_43	Earth Flow	Moderate (11-29)	Pre-Historic (>150yrs)		Tidb	20	30	0	28.2	Deep	1577.5	41349	1165280
PC_44	Complex-Earth Slide-Rotational+Earth Flow	Moderate (11-29)	Pre-Historic (>150yrs)		Tidb, Ty	30	30	25	21.6	Deep	0	180	51350
PC_45	Earth Flow	High (=>30)	Historic (<150yrs)		Tidb	25	15	0	13.6	Deep	135	19844	269628
PC_47	Debris Flow	Low (=<10)	Historic (<150yrs)		Ty	15	0	2	0.0		180	814	543
PC_48	Debris Flow	Low (=<10)	Historic (<150yrs)		Ty	10	0	2	0.0		180	1334	889

Unique_ID	Movement Class	Confidence	Age	Date Last Move	Geology	Slope (°)	Scarp_Height (m)	Fan_Height (m)	Fail_Depth (m)	Deep_Shal	Direction (°)	Area (m^2)	Volume (m^3)
PC_49	Earth Flow	High (=>30)	Historic (<150yrs)		Tidb	25	8	0	3.0	Shallow	90	2164	15682
PC_50	Earth Flow	High (=>30)	Historic (<150yrs)	1999, 2008	Tidb	40	40	4	3.1	Shallow	0	45	28234
PC_51	Earth Flow	Moderate (11-29)	Pre-Historic (>150yrs)		Ty	20	10	0	9.4	Deep	45	62247	584727
PC_52	Earth Flow	Moderate (11-29)	Historic (<150yrs)		Ty	25	6	0	1.5	Shallow	180	2307	12536
PC_53	Earth Flow	Moderate (11-29)	Historic (<150yrs)		Ty	30	8	0	2.5	Shallow	180	3151	21812
PC_54	Earth Flow	Moderate (11-29)	Historic (<150yrs)		Ty	30	4	0	3.5	Shallow	180	1830	6334
PC_55	Earth Flow	Moderate (11-29)	Historic (<150yrs)		Ty	20	6	0	5.6	Deep	90	14481	81619
PC_56	Earth Flow	Moderate (11-29)	Historic (<150yrs)		Ty	20	3	0	2.8	Shallow	90	3022	8517
PC_57	Earth Flow	Moderate (11-29)	Pre-Historic (>150yrs)		Ty	25	15	0	13.6	Deep	22.5	106883	1452240
PC_58	Earth Flow	Moderate (11-29)	Historic (<150yrs)		Ty, Tidb	20	20	20	18.8	Deep	0	315	198248
PC_59	Earth Flow	Moderate (11-29)	Historic (<150yrs)		Tidb, Ty	15	15	30	29.0	Deep	0	225	140953
PC_60	Earth Flow	Moderate (11-29)	Historic (<150yrs)		Ty	30	8	0	2.5	Shallow	45	3756	26004
PC_61	Earth Flow	Moderate (11-29)	Pre-Historic (>150yrs)		Ty, Tidb	28	28	6	5.3	Deep	0	360	30459
PC_62	Earth Flow	Moderate (11-29)	Historic (<150yrs)		Ty	25	8	0	7.2	Deep	360	13442	97410
PC_63	Earth Flow	Moderate (11-29)	Historic (<150yrs)		Ty, Tidb	28	28	6	3.0	Shallow	0	23	7858
PC_64	Earth Flow	Moderate (11-29)	Historic (<150yrs)		Ty, Tidb	22	22	16	2.0	Shallow	0	360	12767
PC_65	Earth Flow	Moderate (11-29)	Historic (<150yrs)		Ty, Tidb	30	30	6	5.2	Deep	0	45	22775
PC_66	Complex-Earth Slide-Rotational+Earth Flow	Moderate (11-29)	Pre-Historic (>150yrs)		Tidb	25	30	0	27.2	Deep	45	102925	2796940
PC_67	Earth Flow	Moderate (11-29)	Pre-Historic (>150yrs)		Tidb	30	50	0	43.3	Deep	45	84730	3665940
PC_68	Earth Flow	Moderate (11-29)	Historic (<150yrs)		Tidb	27	15	0	13.4	Deep	135	55510	741424
PC_69	Complex-Earth Slide-Rotational+Earth Flow	High (=>30)	Pre-Historic (>150yrs)		Tidb	35	50	0	40.9	Deep	112.5	297814	12183800
PC_70	Debris Flow	Moderate (11-29)	Historic (<150yrs)		Tidb	40	0	15	0.0		360	26311	131552
PC_71	Complex-Earth Slide-Rotational+Earth Flow	High (=>30)	Historic (<150yrs)		Tidb, Ty	32	32	40	33.9	Deep	63	315	85664
PC_72	Debris Flow	High (=>30)	Historic (<150yrs)		Tidb	40	0	4	0.0		45	1190	1587
PC_73	Complex-Earth Slide-Rotational+Earth Flow	Moderate (11-29)	Historic (<150yrs)		Tidb	20	25	0	23.5	Deep	112.5	63131	1482580
PC_74	Earth Flow	Moderate (11-29)	Historic (<150yrs)		Tidb	30	30	0	26.0	Deep	157.5	48024	1246690
PC_75	Earth Flow	High (=>30)	Historic (<150yrs)		Tidb	25	25	0	3.0	Shallow	112.5	22916	518931
PC_76	Earth Flow	Moderate (11-29)	Historic (<150yrs)		Tidb	25	14	0	1.5	Shallow	67.5	8874	112537
PC_77	Earth Flow	High (=>30)	Historic (<150yrs)		Tidb	35	6	0	1.0	Shallow	360	400	1965
PC_78	Earth Flow	Moderate (11-29)	Pre-Historic (>150yrs)		Tidb, Ty	15	15	10	2.0	Shallow	0	135	22672
PC_80	Earth Flow	Moderate (11-29)	Historic (<150yrs)		Tidb	25	7	0	2.0	Shallow	270	2605	16518
PC_81	Complex-Earth Slide-Rotational+Earth Flow	Moderate (11-29)	Pre-Historic (>150yrs)		Tidb, Ty	25	25	80	72.5	Deep	80	45	1950330
PC_83	Earth Flow	Moderate (11-29)	Historic (<150yrs)		Tidb	30	10	0	8.7	Deep	22.5	33600	290746
PC_84	Complex-Earth Slide-Rotational+Earth Flow	Moderate (11-29)	Pre-Historic (>150yrs)		Tidb, Ty	35	35	50	40.9	Deep	45	315	155686
PC_85	Complex-Earth Slide-Rotational+Earth Flow	Moderate (11-29)	Historic (<150yrs)		Ty, Tidb	20	20	15	14.1	Deep	38	45	27049
PC_87	Complex-Earth Slide-Rotational+Earth Flow	High (=>30)	Historic (<150yrs)		Ty	25	8	0	7.2	Deep	135	23372	169365
PC_88	Earth Flow	Moderate (11-29)	Historic (<150yrs)		Ty, Tidb	20	20	12	11.3	Deep	0	113	40889
PC_89	Earth Flow	High (=>30)	Historic (<150yrs)		Tidb	25	15	0	13.6	Deep	135	34516	468974
PC_90	Earth Flow	Moderate (11-29)	Historic (<150yrs)		Ty	25	8	0	7.2	Deep	360	76683	555686
PC_91	Earth Flow	Moderate (11-29)	Historic (<150yrs)		Tidb	32	12	0	2.5	Shallow	45	2687	27318
PC_92	Earth Flow	Moderate (11-29)	Historic (<150yrs)		Tidb	25	15	0	4.0	Shallow	45	7592	103150
PC_93	Earth Flow	Moderate (11-29)	Historic (<150yrs)		Tidb	35	25	0	2.5	Shallow	45	5396	110370
PC_95	Earth Flow	Moderate (11-29)	Pre-Historic (>150yrs)		Tidb, Ty	25	25	16	14.5	Deep	0	45	493053
PC_96	Earth Flow	Moderate (11-29)	Pre-Historic (>150yrs)		Ty, Tidb	25	25	8	7.2	Deep	0	23	201706
PC_97	Complex-Earth Slide-Rotational+Earth Flow	Moderate (11-29)	Pre-Historic (>150yrs)		Ty, Tidb	20	20	80	75.1	Deep	163	113	1023140

Unique_ID	Movement Class	Confidence	Age	Date Last Move	Geology	Slope (°)	Scarp_Height (m)	Fan_Height (m)	Fail_Depth (m)	Deep_Shal	Direction (°)	Area (m^2)	Volume (m^3)
PC_98	Debris Flow	Low (=<10)	Historic (<150yrs)		Tidb	10	0	4	0.0		247.5	3436	4581
PC_100	Earth Flow	High (=>30)	Historic (<150yrs)	2007	Tidb	35	3	0	2.5	Shallow	180	3384	8307
PC_101	Earth Flow	High (=>30)	Historic (<150yrs)	2007	Tidb	20	6	0	1.5	Shallow	45	490	2764
PC_102	Earth Flow	High (=>30)	Historic (<150yrs)	2007	Tidb	22	12	0	2.0	Shallow	112.5	5336	59341
PC_103	Earth Flow	High (=>30)	Historic (<150yrs)	2007, 2008	Tidb	40	40	3	2.3	Shallow	0	158	914
PC_104	Earth Flow	High (=>30)	Historic (<150yrs)	2007	Tidb	30	2	0	1.7	Shallow	112.5	1289	2231
PC_105	Debris Flow	High (=>30)	Historic (<150yrs)	2007	Tidb, Ty	45	45	0	3.0	0	0	45	2720
PC_106	Earth Flow	High (=>30)	Historic (<150yrs)	2007, 2008	Tidb	30	30	5	4.3	Shallow	0	113	184
PC_107	Earth Flow	High (=>30)	Historic (<150yrs)		Tidb	40	3	0	2.3	Shallow	292.5	82	187
PC_109	Earth Flow	High (=>30)	Historic (<150yrs)	2007, 2008	Tidb	30	30	5	4.3	Shallow	0	360	1634
PC_111	Earth Flow	High (=>30)	Historic (<150yrs)	2007	Tidb	45	3	0	2.1	Shallow	360	219	463
PC_112	Earth Flow	High (=>30)	Historic (<150yrs)	2007	Tidb	48	3	0	2.0	Shallow	337.5	221	442
PC_113	Earth Slide-Translational	High (=>30)	Historic (<150yrs)	2008	Tidb	38	5	0	3.9	Shallow	247.5	949	3736
PC_115	Earth Flow	High (=>30)	Historic (<150yrs)	2008	Tidb	20	2	0	1.9	Shallow	67.5	132	249
PC_116	Earth Flow	High (=>30)	Historic (<150yrs)	2007, 2008	Tidb	20	20	4	3.8	Shallow	0	68	192
PC_117		High (=>30)	Historic (<150yrs)		Tidb	35	0	0	0.0		67.5	867	0
PC_118	Earth Slide-Rotational	High (=>30)	Historic (<150yrs)	2007	Tidb	41	3	0	2.3	Shallow	45	791	1788
PC_119	Earth Flow	High (=>30)	Historic (<150yrs)		Tidb	40	0	0	0.0		45	738	0
PC_120	Earth Flow	High (=>30)	Historic (<150yrs)		Tidb	35	0	0	0.0		180	327	0
PC_121	Earth Flow	High (=>30)	Historic (<150yrs)	2007	Tidb	45	4	0	2.8	Shallow	45	602	1698
PC_124	Earth Flow	High (=>30)	Historic (<150yrs)	2007	Tidb	35	4	0	3.3	Shallow	360	469	1535
PC_125	Earth Flow	High (=>30)	Historic (<150yrs)	2007	Tidb	30	4	0	3.5	Shallow	337.5	132	456
PC_126	Debris Flow	High (=>30)	Historic (<150yrs)	2007	Tidb	40	0	10	0.0		22.5	740	2467
PC_127	Earth Flow	High (=>30)	Historic (<150yrs)	2008	Tidb	40	10	0	4.0	Shallow	360	4916	37602
PC_128	Earth Flow	Moderate (11-29)	Historic (<150yrs)		Tidb	26	16	0	4.0	Shallow	225	4566	65620
PC_129	Earth Flow	Moderate (11-29)	Historic (<150yrs)		Tidb	40	12	0	2.0	Shallow	360	2343	21501
PC_130	Complex-Earth Slide-Rotational+Earth Flow	Moderate (11-29)	Historic (<150yrs)		Ty	30	14	0	12.1	Deep	22.5	6342	76827
PC_131	Earth Flow	Moderate (11-29)	Pre-Historic (>150yrs)		Ty, Tidb	20	20	25	23.5	Deep	0	23	65861
PC_132	Earth Flow	Moderate (11-29)	Historic (<150yrs)		Tidb	20	8	0	3.0	Shallow	90	19711	148125
PC_133	Earth Flow	High (=>30)	Historic (<150yrs)		Tibd	30	8	0	6.9	Deep	45	9299	64373
PC_134	Earth Flow	Moderate (11-29)	Historic (<150yrs)		Tidb	20	4	0	3.8	Shallow	45	9703	36461
PC_135	Debris Flow	Low (=<10)	Historic (<150yrs)		Ty	15	0	6	0.0		315	1184	2368
PC_136	Debris Flow	Low (=<10)	Historic (<150yrs)		Ty, Tidb	10	10	0	3.0	0	0	315	531
PC_137	Complex-Earth Slide-Rotational+Earth Flow	Moderate (11-29)	Pre-Historic (>150yrs)		Ty, Tidb	20	20	25	23.5	Deep	68	158	59186
PC_138	Earth Flow	Moderate (11-29)	Historic (<150yrs)		Ty	20	10	0	1.0	Shallow	90	1627	15282
PC_139	Earth Flow	Moderate (11-29)	Historic (<150yrs)		Tidb, Ty	25	25	30	27.2	Deep	0	360	24847
PC_140	Earth Flow	Moderate (11-29)	Historic (<150yrs)		Ty, Tidb	20	20	8	3.5	Shallow	0	338	5187
PC_141	Earth Flow	High (=>30)	Historic (<150yrs)		Ty, Tidb	15	15	6	5.8	Deep	0	338	18441
PC_142	Earth Slide-Rotational	Moderate (11-29)	Historic (<150yrs)		Tidb	35	20	0	16.4	Deep	292.5	6457	105668
PC_143	Debris Flow	Moderate (11-29)	Historic (<150yrs)		Tidb	15	0	4	0.0		337.5	2164	2885
PC_144	Earth Flow	Moderate (11-29)	Historic (<150yrs)		Tidb	25	2	0	1.8	Shallow	45	495	897
PC_145	Earth Flow	Moderate (11-29)	Historic (<150yrs)		Tidb	15	6	0	4.0	Shallow	360	3693	21400
PC_146	Earth Slide-Rotational	Moderate (11-29)	Historic (<150yrs)		Tidb	40	40	0	30.6	Deep	45	29814	913660
PC_147	Complex-Earth Slide-Rotational+Earth Flow	Moderate (11-29)	Historic (<150yrs)		Tidb	25	25	0	22.7	Deep	45	50735	1149580
PC_148	Earth Flow	Moderate (11-29)	Historic (<150yrs)		Tidb, Ty	20	20	6	3.0	Shallow	0	45	16774

Unique_ID	Movement Class	Confidence	Age	Date Last Move	Geology	Slope (°)	Scarp_Height (m)	Fan_Height (m)	Fail_Depth (m)	Deep_Shal	Direction (°)	Area (m^2)	Volume (m^3)
PC_149	Earth Flow	Moderate (11-29)	Historic (<150yrs)		Tidb	20	14	0	13.2	Shallow	247.5	2379	31296
PC_150	Earth Flow	Moderate (11-29)	Historic (<150yrs)	1998-2003	Tidb	25	16	0	1.5	Shallow	247.5	3909	56693
PC_151	Complex-Earth Slide-Rotational+Earth Flow	Moderate (11-29)	Historic (<150yrs)	1998-2003	Tidb	25	12	0	10.9	Deep	22.5	6682	72676
PC_152	Debris Flow	Moderate (11-29)	Historic (<150yrs)	2003-2005	Tidb	20	0	6	0.0		22.5	1317	2634
PC_153	Earth Flow	Moderate (11-29)	Historic (<150yrs)		Tidb	30	4	0	3.5	Shallow	67.5	1120	3880
PC_154	Earth Flow	Moderate (11-29)	Historic (<150yrs)		Tidb	25	6	0	2.5	Shallow	135	4096	22272
PC_155	Earth Flow	High (=>30)	Historic (<150yrs)	2007	Ty	25	3	0	2.7	Shallow	45	662	1800
PC_156	Earth Slide-Rotational	High (=>30)	Historic (<150yrs)	2007, 2008	Ty	25	25	8	7.2	Deep	0	135	6197
PC_157	Earth Flow	Moderate (11-29)	Historic (<150yrs)		Tidb, Ty	20	20	4	3.8	Shallow	0	158	8313
PC_158	Earth Flow	Moderate (11-29)	Historic (<150yrs)		Tidb	40	4	0	3.1	Shallow	337.5	1579	4839
PC_159	Earth Flow	Moderate (11-29)	Historic (<150yrs)		Tidb	40	7	0	3.0	Shallow	360	2746	14729
PC_160	Complex-Earth Slide-Rotational+Earth Flow	Moderate (11-29)	Pre-Historic (>150yrs)		Ty, Tidb	20	20	7	6.6	Deep	0	360	24425
PC_161	Earth Flow	High (=>30)	Historic (<150yrs)	2007	Tidb	40	1	0	0.8	Shallow	45	201	154
PC_162	Debris Flow	High (=>30)	Historic (<150yrs)	2007	Tidb	30	0	3	0.0		315	594	594
PC_163	Debris Flow	High (=>30)	Historic (<150yrs)	2007	Tidb	35	0	1	0.0		22.5	187	62
PC_164	Debris Flow	High (=>30)	Historic (<150yrs)	2007	Tidb	35	0	1.5	0.0		22.5	231	115
PC_165	Earth Flow	High (=>30)	Historic (<150yrs)	1988-2003	Tidb	35	3	0	2.5	Shallow	180	633	1556
PC_166	Earth Flow	High (=>30)	Historic (<150yrs)	1988-2003	Tidb	30	6	0	4.0	Shallow	360	1447	5791
PC_167	Earth Flow	High (=>30)	Historic (<150yrs)	2003-2005	Tidb	40	2	0	1.5	Shallow	22.5	123	189
PC_168	Debris Flow	High (=>30)	Historic (<150yrs)	Before 1970	Tidb, Ty	20	0	2	0.0		189	3223	2148